Chapter 3

PLL Based Control Strategy of a Grid-Tied PV System Under Distorted Grid Voltage Conditions

3.1 Introduction

The previous chapter presents grid-tied PV system operated with coordinated control strategy along with the implementation of proposed capability curve under maximum power point condition. In recent times, the increase of nonlinear loads, such as electronic devices in the grid-tied PV system are remarkable. As these loads inject harmonic currents, the harmonic content in the grid voltage also increases. The coordinated control strategy presented in the previous chapter, which uses PI controller, cannot mitigate the grid current harmonics and power oscillations under distorted grid voltages. This chapter presents an advanced integrated control strategy for mitigating grid current harmonics and power ripple eliminations in grid-tied PV systems under distorted grid voltage conditions. The proposed control strategy consists of an advanced proportional multi resonant (APMR) current controller and a compensator for grid voltage sag (CGVS), which is implemented using a phase-locked loop (PLL) block. The CGVS and the APMR eliminate the active and reactive power ripples under unbalanced voltage sag conditions. Further, an adaptive step size incremental conductance (ASINC) maximum power point tracking (MPPT) controller is used to integrate the proposed control strategy. Along with current harmonic reduction (by APMR controller), the ASINC method ensures effective and faster tracking of maximum power point (MPP) and ensures negligible oscillations in the steady-state under different environmental conditions. By utilizing the proposed APMR control strategy, the frequency adaptability of the grid-tied PV system is improved compared to the conventional proportional multi resonant (CPMR) control strategy under grid frequency deviations. The proposed control strategy of APMR with CGVS almost completely eliminates the power ripples under even severe unbalanced voltage sag conditions. Experimental studies are carried out using a real-time digital simulator (OPAL-RT OP-4510) to verify the proposed control strategy's effectiveness compared to the conventional PMR (CPMR) controller.

3.2 System Architecture of the Grid-Tied PV System

The schematic diagram of a three-phase grid-tied PV system with the proposed control strategy of APMR with CGVS is shown in Fig. 3.1. The PV array is connected to the grid through a VSI and a LCL filter at the point of interconnection. The control strategy of the grid-tied PV system is designed to inject a sinusoidal grid current under distorted grid voltage conditions. The grid-tied PV system control architecture, as shown in Fig. 3.1, has four significant parts: 1) ASINC MPPT controller, 2) DC-link voltage controller, 3) proposed APMR current controller, and 4) PLL based grid synchronization with CGVS. A feedback linearization (FBL) method-based DC-link voltage controller is used to control the PV array DC output voltage according to the reference given by the MPPT controller. The proposed APMR current controller regulates the grid injected current with enhanced harmonic compensation. The grid injected current is controlled according to the PV array real power output and the required reactive power. The MPPT controller based on the ASINC method is used in this work to track the MPP with negligible steady-state oscillations and faster speed than the conventional INC method. The CGVS integrated PLL-based grid synchronization method synchronizes the PV system to the grid. The CGVS, along with the APMR controller, helps to eliminate the power ripples in voltage sag conditions. A detailed discussion of the proposed scheme of APMR current controller with grid synchronization with CGVS is presented in section 3.3. The DC-link voltage controller and the MPPT controller are explained in the following subsections.

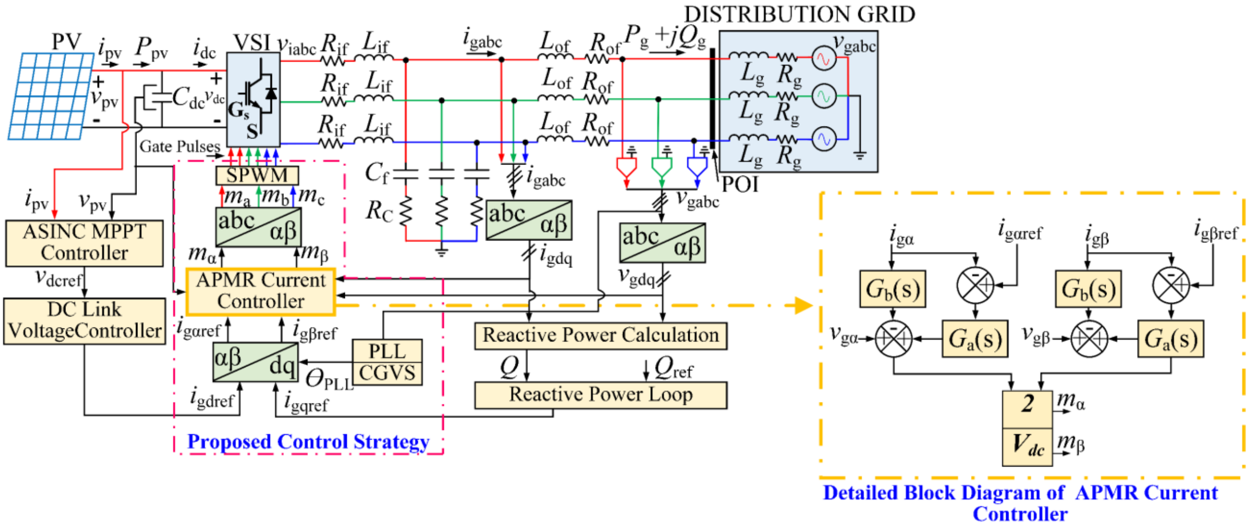

Fig. 3.1. Schematic diagram of the three-phase grid-tied PV system with the proposed control strategy of APMR with CGVS.

3.2.1 DC-link Voltage Controller Design

The objective of the DC-link voltage controller is to regulate the DC-link voltage at a desirable level which is necessary for maintaining stability in the grid-tied PV system. Fig. 3.2 depicts the block diagram of the DC link voltage controller. The DC-link voltage controller is designed by using the dynamics of stored energy in the DC-link capacitor, which controls the active power of the DC-link capacitor. The mathematical model illustrating the voltage dynamics of the DC-link capacitor is based on the principle of electrical power balance. The active power P_{grid} injected into the grid is given by

$$P_{\text{grid}} = P_{\text{PV}} - C_{\text{dc}} v_{\text{dc}} \frac{dv_{\text{dc}}}{dt} \tag{3.1}$$

where $P_{\text{grid}} = (3/2)\, v_{\text{gd}} i_{\text{gd}}$ and $P_{\text{PV}} = \text{v}_{\text{PV}}\text{i}_{\text{PV}}$. The expression given in (3.1) can be simplified as

$$C_{\text{dc}} \frac{dv_{\text{dc}}}{dt} = i_{\text{PV}} - \frac{3 v_{\text{gd}} i_{\text{gd}}}{2 v_{\text{dc}}} \tag{3.2}$$

where i_{gd} and v_{gd} denote the d-axis grid current and voltage; v_{dc} and i_{PV} are DC-link voltage and PV current, respectively.

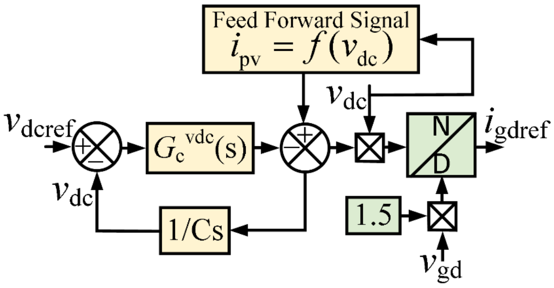

Fig. 3.2. Block diagram of the DC-link voltage controller.

According to the FBL technique, (3.2) can be expressed in the following form

$$\dot{x} = f(x) + g(x)u_{\text{i}} \tag{3.3}$$

where $f(x)$ and $g(x)$ are the nonlinear functions of a system hiving x states and u_i control inputs.

Using the control input u_{i}, the expression given in (3.3) can be written as

$$u_{\text{i}} = \frac{1}{g(x)}[u_{\text{v}} - f(x)] \tag{3.4}$$

The nonlinearities can be canceled out as

$$\dot{x} = u_{\text{v}} \tag{3.5}$$

Considering i_{gd} as a new control input, it can be expressed into a simple LTI system as follows

$$C_{\text{dc}} \frac{dv_{\text{dc}}}{dt} = u_{\text{v}} \tag{3.6}$$

From (3.6), the plant transfer function is derived as

$$G_{\mathrm{p}}(s) = \frac{v_{\mathrm{dc}}(s)}{u_{\mathrm{v}}(s)} = \frac{1}{sC_{\mathrm{dc}}} \tag{3.7}$$

For the preceding plant transfer function $G_p(s)$, a PI controller $G_{\mathrm{c}}^{\mathrm{vdc}}(s)$ is designed

$$\frac{du_{\mathrm{v}}}{dt} = K_{\mathrm{pv_{dc}}}(v_{\mathrm{dcref}} - v_{\mathrm{dc}}) + K_{\mathrm{iv_{dc}}} \int (v_{\mathrm{dcref}} - v_{\mathrm{dc}})\, dt \tag{3.8}$$

where v_{dcref} is the reference value of the DC-link voltage; K_{pvdc} and K_{ivdc} are the proportional and integral gains of the DC-link voltage controller $G_{\mathrm{c}}^{\mathrm{vdc}}(s)$.

3.2.2 Adaptive Step Size INC MPPT Controller Design

The PV array's efficiency and economic performance are increased by using an MPPT controller to extract maximum PV power. The two most popular MPPT methods widely used are perturbed and observe and incremental conductance (INC) methods. However, steady-state oscillation and slow dynamic response are recognized as the significant disadvantages of these methods with fixed step size. There is a tradeoff between steady-state oscillations and tracking speed during change in environmental conditions with fixed step size INC (FSINC) method. Therefore, the tracking is not proper for the FSINC method with a small MPPT sampling time (0.02 s). For proper MPPT with FSINC, the required sampling time increases (0.06 s), and thus the total tracking time increases with fixed step size. As a solution, an adaptive step size incremental conductance (ASINC) MPPT method with variable voltage step size and MPPT sampling time (0.06 s) is used to achieve fast and accurate MPP. The step size is automatically adjusted depending on the slope ($dp_{\mathrm{PV}}/dv_{\mathrm{PV}}$) of the PV array's voltage versus power characteristics. The ASINC MPPT allows very fast-tracking of the MPP with more significant voltage steps, when the operating point is far from MPP. When the operating point is close to the MPP, the step size becomes very small, and the oscillations around the MPP is almost negligible. The slope of the PV characteristics should be zero to achieve MPP, and it is mathematically expressed by

$$\frac{dp_{pv}}{dv_{pv}} = \frac{d(i_{pv} * v_{pv})}{dv_{pv}} = i_{pv} + v_{pv}\frac{di_{pv}}{dv_{pv}} = 0\,. \tag{3.9}$$

The condition for the ASINC MPPT from (3.9) is expressed as

$$\left.\begin{array}{lll}
\dfrac{di_{pv}}{dv_{pv}} + \dfrac{i_{pv}}{v_{pv}} = 0; & \dfrac{dp_{pv}}{dv_{pv}} = 0, & \text{at MPP} \\[2ex]
\dfrac{di_{pv}}{dv_{pv}} + \dfrac{i_{pv}}{v_{pv}} > 0; & \dfrac{dp_{pv}}{dv_{pv}} > 0, & \text{at right of MPP} \\[2ex]
\dfrac{di_{pv}}{dv_{pv}} + \dfrac{i_{pv}}{v_{pv}} < 0; & \dfrac{dp_{pv}}{dv_{pv}} < 0, & \text{at left of MPP}
\end{array}\right\} \tag{3.10}$$

The variable step size S_{step} depends on the slope of the PV characteristics and it is expressed as

$$S_{\mathrm{step}} = n\left|\frac{v_{\mathrm{pv}}(k)i_{\mathrm{pv}}(k) - v_{\mathrm{pv}}(k-1)i_{\mathrm{pv}}(k-1)}{v_{\mathrm{pv}}(k) - v_{\mathrm{pv}}(k-1)}\right| \tag{3.11}$$

where i_{pv}(k) and v_{pv}(k) are the PV array current, and voltage at k$^{\mathrm{th}}$ sampling instant and n is the scaling coefficient.

3.3 Proposed Control Strategy

This section proposes a control strategy of APMR with CGVS to suppress the grid current harmonics and power ripples of a grid-tied PV system under distorted grid voltage conditions. The proposed control strategy is divided into two segments. The first segment is the APMR controller, which is utilized for current harmonic compensation. The second segment is the CGVS in integration with PLL and APMR controller and is used for power ripples mitigation. The detailed discussion of the difference between the conventional PMR and the proposed APMR controller is presented in sections 3.3.1 and 3.3.2. The frequency response analysis of the proposed APMR is presented in section 3.3.2. The advantages of the proposed APMR controller over the conventional PMR are also discussed in this section.

3.3.1 The Conventional Proportional Multi-Resonant Controller

The conventional proportional resonant (PR) controller easily tracks the grid current's fundamental component along with zero steady-state error [113]. The control structure block diagram of the conventional proportional multi resonant (CPMR) current controller is shown in Fig. 3.4. The error between the reference grid current and the measured grid current signals is processed by a proportional resonant compensator (PRC) G_{ac}(s). A resonant harmonic compensator (RHC) G_{bc}(s) is connected in parallel to PRC. The PRC ensures the accurate tracking of the fundamental component of grid current reference and the RHC compensates the selected grid current harmonics. The transfer function of G_{ac}(s) and G_{bc}(s) can be expressed as

$$\left.\begin{aligned} G_{\mathrm{ac}}(s) &= K_{\mathrm{p}} + \frac{K_{\mathrm{r}}s}{s^2+{\omega_{\mathrm{g}}}^2} \\ G_{\mathrm{bc}}(s) &= \sum_{\mathrm{h}=5,7,11,\ldots} \frac{K_{\mathrm{rh}}s}{s^2+(h\omega_{\mathrm{g}})^2} \end{aligned}\right\} \tag{3.12}$$

where K_p and K_r are the proportional coefficients, fundamental resonant coefficient of the CPMR controller; K_{rh} is the resonant controller coefficients of the order h; ω_g and h denote the resonant frequency and harmonic order of the conventional PMR, respectively. A simplified model of the three-phase grid-tied PV system is shown in Fig. 3.4. In Fig. 3.4, Z_{if}, Z_{og}, and Z_c denote simplified impedances of the inverter side series impedance, grid side impedance, and shunt impedance of the filter, respectively. The modulating signals of the inverter in *αβ* reference frame obtained from Fig. 3.3 are expressed as

$$m_{\alpha\beta} = \frac{2}{v_{dc}}[v_{g\alpha\beta} + \{G_{ac}(s) + G_{bc}(s)\}(i_{g\alpha\beta ref} - i_{g\alpha\beta})] \tag{3.13}$$

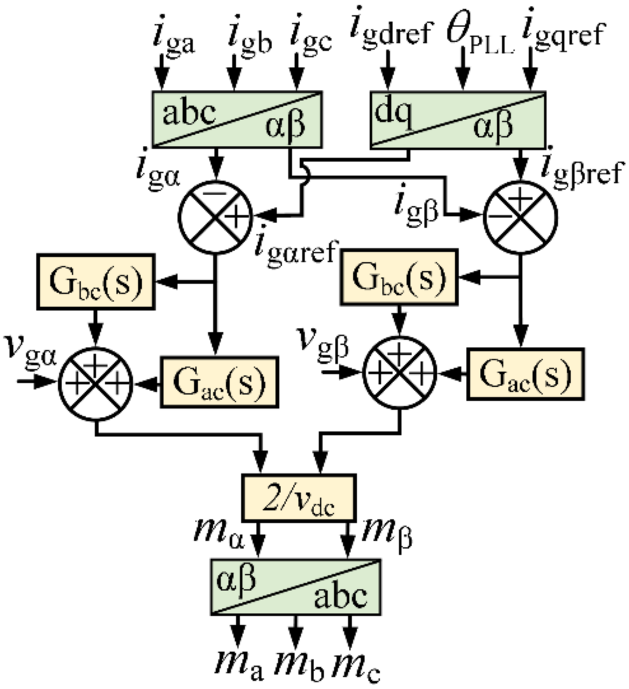

Fig. 3.3. Control structure block diagram of the CPMR current controller.

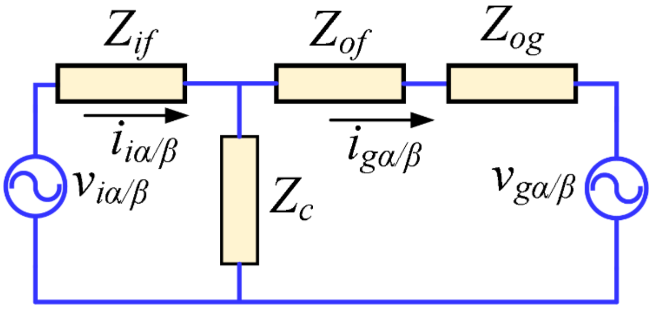

Fig. 3.4. A simplified model of the grid-tied PV system.

The inverter output voltage $v_{i\alpha\beta}$ is expressed as

$$v_{i\alpha\beta} = \frac{v_{dc}}{2} m_{\alpha\beta} \tag{3.14}$$

Using the expression given in (3.13), (3.14) and Fig. 3.4, the grid voltage $v_{g\alpha\beta}$, inverter voltage $v_{i\alpha\beta}$, and the inverter current $i_{i\alpha\beta}$ can be derived as

$$\left.\begin{aligned} v_{\mathrm{g\alpha\beta}} &= \frac{v_{\mathrm{i\alpha\beta}}}{2} - Z_{\mathrm{if}}(s)i_{\mathrm{i\alpha\beta}} - \left\{Z_{\mathrm{g}}(s)+Z_{of}(s)\right\} i_{\mathrm{g\alpha\beta}} \\ v_{\mathrm{i\alpha\beta}} &= \frac{2}{m_{\alpha\beta}}\left(Z_{\mathrm{if}}(s)i_{\mathrm{i\alpha\beta}} + Z_{\mathrm{c}}(s)(i_{\mathrm{i\alpha\beta}} - i_{\mathrm{g\alpha\beta}})\right) \\ i_{\mathrm{i\alpha\beta}} &= \left(\frac{\left\{Z_{\mathrm{of}}(s)+Z_{\mathrm{g}}(s)\right\} i_{\mathrm{g\alpha\beta}} + v_{\mathrm{g\alpha\beta}}}{Z_{\mathrm{c}}(s)}\right) + i_{\mathrm{g\alpha\beta}} \end{aligned}\right\} \tag{3.15}$$

By substituting (3.15) in (3.13), the transfer function of the CPMR controller is expressed as,

$$i_{\mathrm{g\alpha\beta}}(s) = g_{\mathrm{r}}(s)i_{\mathrm{g\alpha\beta ref}}(s) + g_{\mathrm{g}}(s)v_{\mathrm{g\alpha\beta}}(s) \tag{3.16}$$

The detailed expression of the transfer function $g_r(s)$ and $g_g(s)$ can be written as

$$\left.\begin{aligned} g_{\mathrm{r}}(s) &= \frac{i_{\mathrm{g\alpha\beta}}(s)}{i_{\mathrm{g\alpha\beta ref}}(s)} = \frac{Z_{\mathrm{c}}(s)\left\{G_{\mathrm{ac}}(s)+G_{\mathrm{bc}}(s)\right\}}{Z_{\mathrm{if}}(s)(Z_{\mathrm{c}}(s)+Z_{\mathrm{of}}(s)+Z_{\mathrm{og}}(s))+(Z_{\mathrm{c}}(s)+Z_{\mathrm{of}}(s)+Z_{\mathrm{og}}(s))(G_{\mathrm{ac}}(s)+G_{\mathrm{bc}}(s))} \\ g_{g}(s) &= \frac{i_{\mathrm{g\alpha\beta}}(s)}{v_{\mathrm{g\alpha\beta}}(s)} = -\frac{Z_{\mathrm{if}}(s)+G_{\mathrm{ac}}(s)+G_{\mathrm{bc}}(s)}{Z_{\mathrm{if}}(s)(Z_{\mathrm{c}}(s)+Z_{\mathrm{of}}(s)+Z_{\mathrm{og}}(s))+(Z_{\mathrm{c}}(s)+Z_{\mathrm{of}}(s)+Z_{\mathrm{og}}(s))(G_{\mathrm{ac}}(s)+G_{\mathrm{bc}}(s))} \end{aligned}\right\} \tag{3.17}$$

where g_{r} (s) is the system's closed-loop transfer function between $i_{\mathrm{g\alpha\beta}}$ and $i_{\mathrm{g\alpha\beta ref}}$, and g_{g} (s) is the closed-loop transfer function between $i_{\mathrm{g\alpha\beta}}$ and $v_{\mathrm{g\alpha}}$.

Fig. 3.5 shows the bode diagram of G_{ac} (s), G_{bc}(s) and closed-loop transfer function g_{r} (s) for a conventional PMR controller. It is observed from Fig. 3.5 (a) that the magnitude of G_{ac} (s) at the resonant frequency (50 Hz) is very high (infinite). The transfer function introduces narrow magnitude peaks at the selected harmonic frequencies 250 Hz, 350 Hz, 550 Hz, 650 Hz, 850 Hz and 950 Hz. It is noticed from Fig. 3.5 (b) that the transfer function g_{r} (s) has a minimal attenuation in the magnitude diagram at the selected harmonic frequencies. A flat unity gain is noticed at the wide frequency range. This flat unity gain and zero-phase characteristics are suitable for tracking the fundamental grid current reference signal. However, the attenuation of the selected harmonics are not significant.

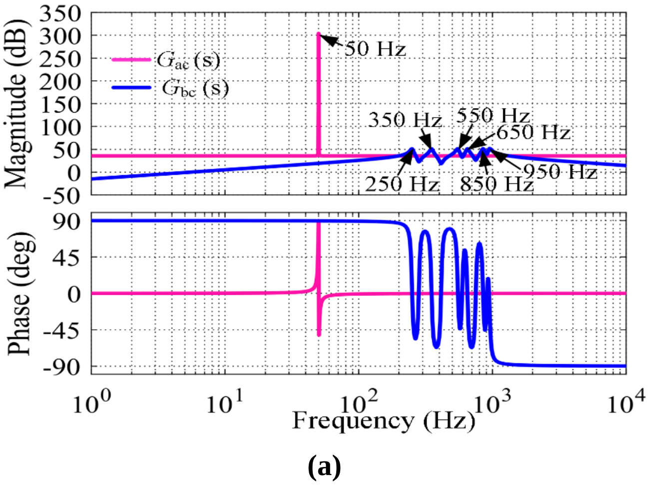

(a)

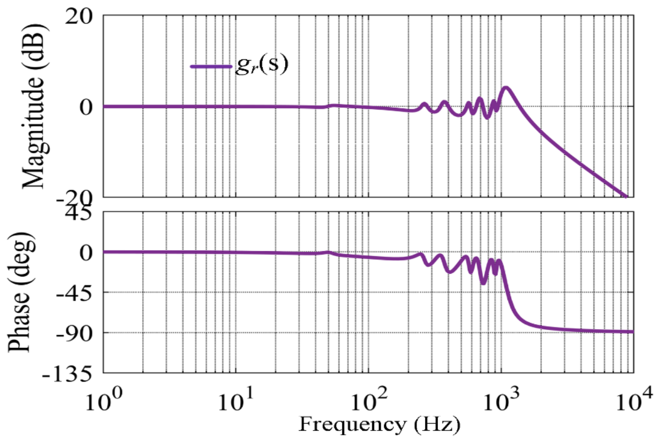

(b)

Fig. 3.5. Bode diagrams of **(a)** $G_{ac}(s)$ and $G_{bc}(s)$ **(b)** closed-loop transfer functions $g_r(s)$ ($K_p = 30$, $K_r = 250$ and $\xi=0.02$) with conventional PMR controller.

3.3.2 The Proposed Advanced Proportional Multiresonant Controller

For harmonic compensation, the conventional proportional multi resonant (PMR) controller can be used as a current controller in the grid-tied PV system. It can easily track the grid current's fundamental component along with zero steady-state error [114]. However, it has drawbacks such as infinite gain at resonant frequency, narrow bandwidth and sensitive to grid frequency deviations. The controller with an infinite gain is challenging to realize and difficult to implement practically. Due to the infinite gain, the conventional PMR controller is sensitive to the resonant frequency, leading to the chances of becoming unstable. Also, the conventional PMR controller cannot suppress the grid current harmonics under highly distorted grid voltages. Moreover, the bandwidth of the conventional PMR is very narrow around the resonant frequency. Due to this narrow bandwidth around resonant frequency, the conventional PMR is not suitable for accurate digital implementation. Therefore, to overcome the problems mentioned above, an advanced proportional resonant (APMR) controller with a modified control structure is proposed having different transfer functions of PRC and RHC. In addition, a damping factor (ξ) is introduced in the transfer function of the conventional PMR controller to obtain the desired transfer functions of APMR controller. Thus, the APMR controller has finite gain, improved transient response and stability. Also, it is it easier for digital implementation.

The proposed APMR controller's main objective is to regulate the injected grid current with reduced total harmonic distortion (THD) and to provide a smooth and sinusoidal current without grid voltage distortions. The representative schematic diagram and the control block diagram of the proposed APMR current controller are shown in Fig. 3.6(a) and Fig. 3.6(b), respectively. Fig 3.6(a) illustrates the detailed APMR structure along with other controllers of the system. In the representative block diagram of APMR controller, i_{gdref} and i_{gqref} are obtained from the output of reactive power loop and the DC-link voltage controller. The proposed APMR controller consists of two compensators, named as proportional resonant compensator (PRC) and resonant harmonic compensator (RHC) with transfer function $G_{\mathrm{a}}(s)$ and $G_{\mathrm{b}}(s)$, respectively. The PRC is used to eliminate the steady-state error, when tracking a sinusoidal signal with zero steady-state error. However, it cannot suppress the low-order harmonics. Therefore, an additional compensator, RHC is connected in parallel with the PRC. The RHC aims to compensate the system harmonics at the selected harmonic frequencies.

The TF of PRC and RHC are expressed as $G_{\mathrm{a}}(s)$ and $G_{\mathrm{b}}(s)$, respectively are as follows

$$G_{\mathrm{a}}(s) = \frac{2K_{\mathrm{r}}\xi\omega_{\mathrm{g}}s}{s^2 + 2\xi\omega_{\mathrm{g}}s + \omega_{\mathrm{g}}{}^2} \tag{3.18}$$

$$G_{\mathrm{b}}(s) = K_{\mathrm{p}} + \sum_{\mathrm{h}=5,7,11,\ldots} \frac{2K_{\mathrm{rh}}\xi(h\omega_{\mathrm{g}})s}{s^2 + 2\xi(h\omega_{\mathrm{g}})s + (h\omega_{\mathrm{g}})^2} \tag{3.19}$$

where K_{p} and K_{r} are the proportional coefficients, fundamental resonant coefficient of the APMR controller; K_{rh} is the resonant controller coefficients of the order h; ω_{g} and h denote the resonant frequency and harmonic order of the proposed APMR controller; ξ is the damping factor of the APMR controller, respectively.

It can be noted that the PRC includes only the fundamental resonant term and the RHC includes both the proportional and resonant harmonic terms. The APMR controller is used to regulate the grid current reference value by processing the grid current error $i_{\mathrm{g\alpha\beta ref}}$ -$i_{\mathrm{g\alpha\beta}}$ applied to the input of G_{a} (s). The injected grid current $i_{\mathrm{g\alpha\beta}}$ is applied to the input of G_{b} (s) as shown in Fig. 3.6(b). The output of the APMR controller is multiplied by $2/v_{\mathrm{dc}}$ to obtain the signals m_α and m_β. Moreover, these signals are converted into three-phase modulating signals m_{a}, m_{b} and m_{c}.

The property of enhanced harmonic compensation of the proposed AMPR controller is based on the following two facts.

Fact 1: The proposed APMR controller with transfer function G_{a} (s) tracks the fundamental reference current with zero steady-state error.

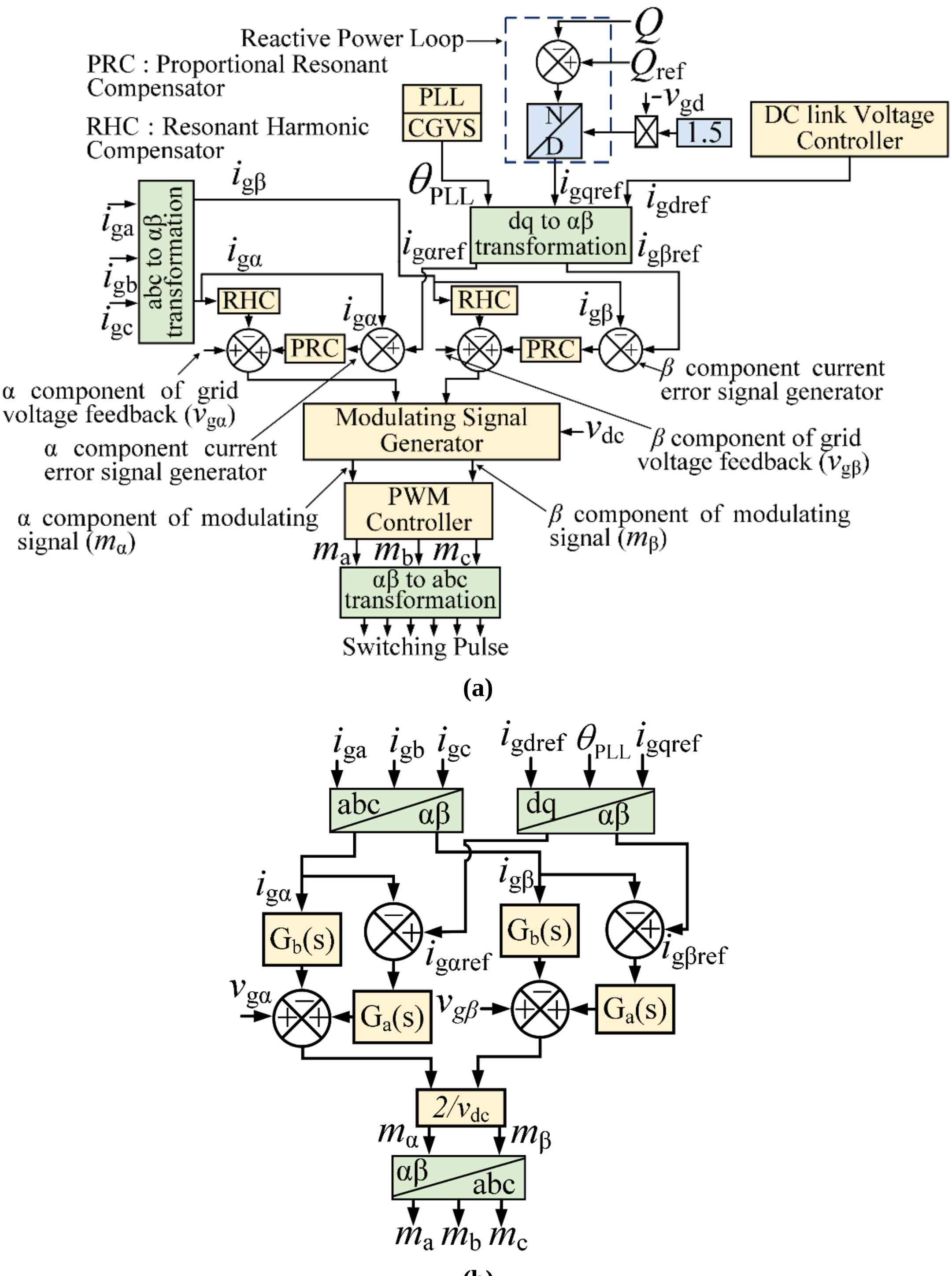

(a)

(b)

Fig. 3.6. Detailed diagram of the proposed APMR current controller **(a)** representative block diagram, **(b)** control structure with transfer function.

Fact 1 is due to the presence of $s^2+2\xi\omega_g s+(\omega_g)^2$ in the denominator of the transfer function G_a (s) in (3.18). This term is a second-order integrator, which guarantees that the steady-state error is eliminated. Moreover, it is seen from (3.18) that at $s = j\omega_g$, the transfer function behaves like a notch filter with finite high gain at fundamental grid frequency (ω_g). Due to this behavior, the steady-state error becomes zero.

Fact 2: The transfer function $G_{\mathrm{b}}(\mathrm{s})$ eliminates the system's selected harmonics under distorted grid voltages with various harmonic ripples.

Due to the presence of $\mathrm{s}^2+2\xi n\omega_{\mathrm{g}}\mathrm{s}+(h\omega_{\mathrm{g}})^2$ in the denominator of the transfer function $G_{\mathrm{b}}(\mathrm{s})$ in (3.19), the grid current harmonics ($h\omega_{\mathrm{g}}$) to be eliminated are selected. It can be noticed from Fig. 3.6 (b) that the output of G_{b} (s) is subtracted from the output of G_{a} (s). Thus, the complete APMR removes the selected harmonics from the output of $G_{\mathrm{a}}(\mathrm{s})$. The proposed APMR controller can successfully track the fundamental component of grid current and eliminate the selected harmonic frequencies in grid current under distorted grid voltages.

3.3.2.1 Frequency Response Analysis of the Proposed APMR Controller

This section illustrates the frequency response analysis of the proposed APMR controller. The modulating signals of the inverter obtained from Fig. 3.6 (b) is expressed as

$$m_{\alpha/\beta}=\frac{2}{v_{\mathrm{dc}}}[v_{\mathrm{g}\alpha/\beta}+G_{\mathrm{a}}(s)(i_{\mathrm{g}\alpha/\beta\mathrm{ref}}-i_{\mathrm{g}\alpha/\beta})-G_{\mathrm{b}}(s)i_{\mathrm{g}\alpha/\beta}] \tag{3.20}$$

By substituting (3.15) in (3.20), the transfer function of the APMR controller is obtained as

$$i_{\mathrm{g}\alpha\beta}(s)=g_{\mathrm{r}}(s)i_{\mathrm{g}\alpha\beta\mathrm{ref}}(s)+g_{\mathrm{g}}(s)v_{\mathrm{g}\alpha\beta}(s) \tag{3.21}$$

The detailed expression of the transfer function $g_{\mathrm{r}}(\mathrm{s})$ and $g_{\mathrm{g}}(\mathrm{s})$ can be expressed as

$$\left.\begin{aligned} g_{\mathrm{r}}(s)&=\frac{i_{\mathrm{g}\alpha\beta}(s)}{i_{\mathrm{g}\alpha\beta\mathrm{ref}}(s)}=\frac{Z_{\mathrm{c}}(s)G_{\mathrm{a}}(s)}{Z_{\mathrm{if}}(s)(Z_{\mathrm{c}}(s)+Z_{\mathrm{of}}(s)+Z_{\mathrm{og}}(s))+(Z_{\mathrm{c}}(s)+Z_{\mathrm{of}}(s)+Z_{\mathrm{og}}(s))(G_{\mathrm{a}}(s)+G_{\mathrm{b}}(s))}\\ g_{g}(s)&=\frac{i_{\mathrm{g}\alpha\beta}(s)}{v_{\mathrm{g}\alpha\beta}(s)}=-\frac{Z_{\mathrm{if}}(s)+G_{\mathrm{a}}(s)+G_{\mathrm{b}}(s)}{Z_{\mathrm{if}}(s)(Z_{\mathrm{c}}(s)+Z_{\mathrm{of}}(s)+Z_{\mathrm{og}}(s))+(Z_{\mathrm{c}}(s)+Z_{\mathrm{of}}(s)+Z_{\mathrm{og}}(s))(G_{\mathrm{a}}(s)+G_{\mathrm{b}}(s))}\end{aligned}\right\} \tag{3.22}$$

where g_{r} (s) is the system's closed-loop transfer function between $i_{\mathrm{g}\alpha\beta}$ and $i_{\mathrm{g}\alpha\beta\mathrm{ref}}$, and g_{g} (s) is the closed-loop transfer function between $i_{\mathrm{g}\alpha\beta}$ and $v_{\mathrm{g}\alpha\beta}$.

The Bode diagrams of $G_{\mathrm{a}}(\mathrm{s})$ and $G_{\mathrm{b}}(\mathrm{s})$ for the APMR current controller and closed-loop transfer function g_{r} (s) with different K_{p} and fixed ξ and K_{r} are shown in Fig. 3.7. It is observed from Fig. 3.7 (a) that the gain of $G_{\mathrm{a}}(\mathrm{s})$ at the designed resonant frequency (50 Hz) is above 40 dB. The peak in the magnitude plots for $G_{\mathrm{b}}(\mathrm{s})$ occurs at selected frequencies 250 Hz, 350 Hz, 550 Hz, 650 Hz, 850 Hz, and 950 Hz. It is noticed that the peaks of the magnitude plots of $G_{\mathrm{b}}(\mathrm{s})$ increase with increase in K_{p}. As K_{p} increases, the peak value of the magnitude plots of $g_{\mathrm{r}}(\mathrm{s})$ decreases, as presented in Fig. 3.7 (b). It is seen that a smaller K_{p} value is used to ensure excellent harmonic current tracking performance. Therefore, the grid current harmonics at these selected frequencies are eliminated.

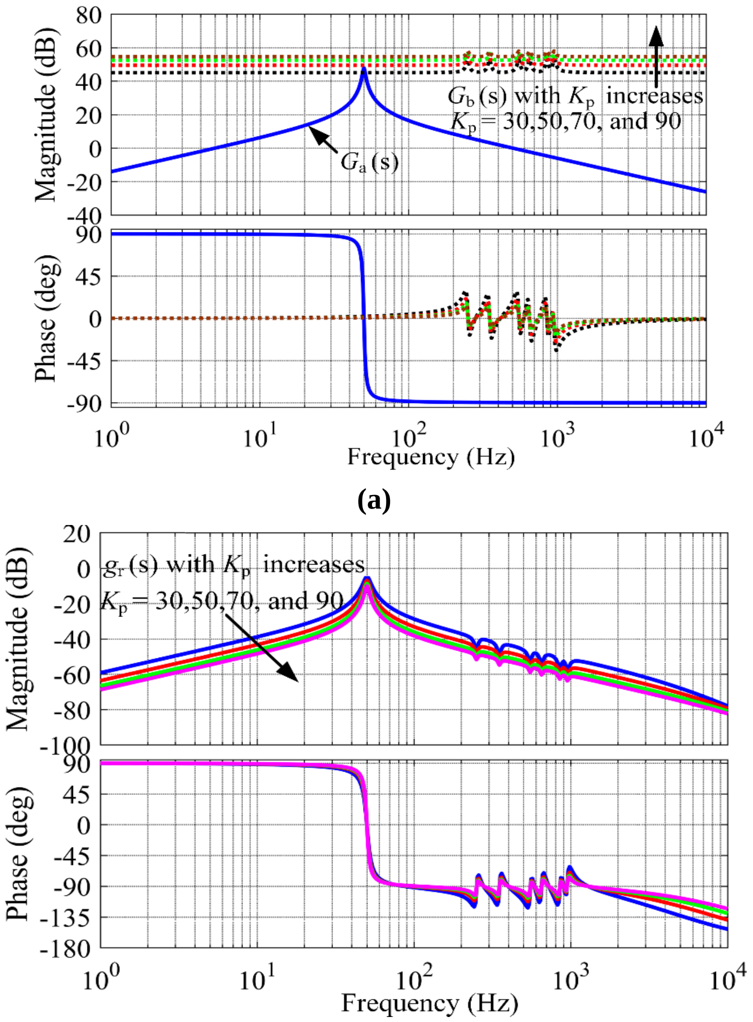

(a)

(b)

Fig. 3.7. Bode diagrams of **(a)** G_a(s) and G_b(s) **(b)** closed loop transfer functions g_r(s) with different K_p values (K_r = 250, ξ = 0.02).

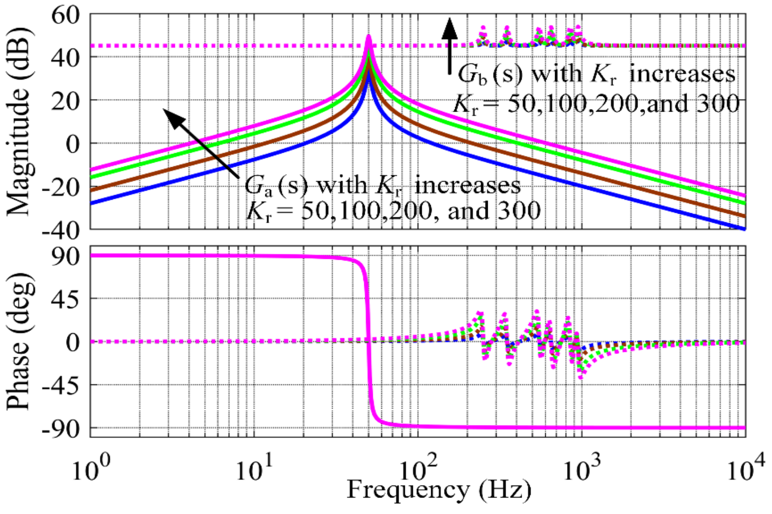

(a)

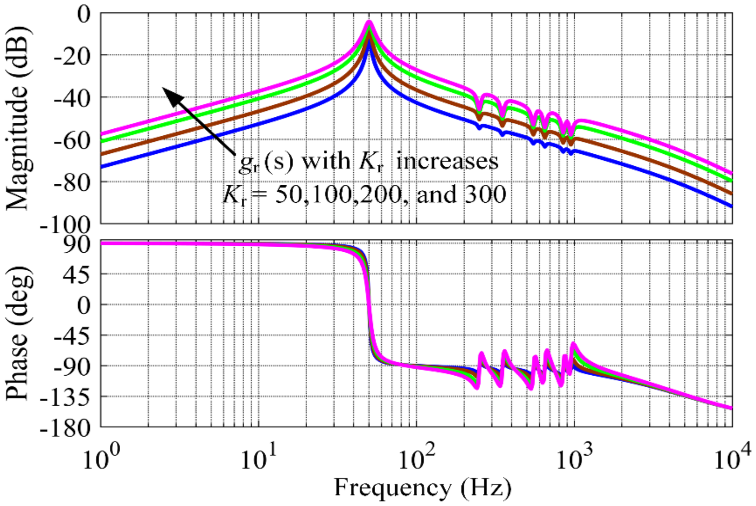

(b)

Fig. 3.8. Bode diagrams of **(a)** G_a (s) and G_b(s) **(b)** closed loop transfer functions g_r (s) with different K_r values (K_p= 30, ξ= 0.02).

The Bode diagram of G_a(s) and G_b(s) for the APMR controller and closed-loop transfer function g_r (s) with different K_r and fixed K_p and ξ are shown in Fig. 3.8. It is seen from Fig. 3.8(a) that for an increase in the values of K_r, the peak magnitude of G_a(s) at the resonant frequency (50 Hz) increases. Such an increase in magnitude broadens the bandwidth of the APMR controller. Therefore, the wider bandwidth is helpful to improve the adaptability of variations in frequency around grid frequency. The grid current harmonic rejection capability of the APMR controller improves in this way. Also, the closed-loop transfer function g_r (s) attains unity gain at the fundamental resonant frequency as demonstrated in Fig. 3.8(b). The larger value of K_r is to provide better steady-state performance for harmonic current compensation. Fig. 3.9 shows the bode diagram of G_a(s) and G_b(s) for the APMR controller and transfer function g_r (s) with different values of ξ with fixed K_p and K_r. It can be noticed from Fig. 3.9(a) that as the value of ξ increases, the peaks from the bode diagram of G_a(s) and G_b(s) disappear, thus reduces the attenuation of the selected harmonics. The approximate selection of ξ helps to increase the bandwidth and decrease the sensitivity during the frequency variation in the grid. As the value of ξ increases, the bode plot's peak magnitude disappears, reducing the selected harmonics attenuation as illustrated in Fig. 3.9(b). Therefore, the values of ξ should be kept low for adequate harmonic compensation. For proper operation of the APMR controller, the values of K_p, K_r and ξ are selected as 30, 250 and 0.02. The Bode diagram of APMR controller and transfer function g_r(s) for K_p = 30, K_r = 250 and ξ = 0.02 is shown in Fig. 3.10. It can be noticed from Fig. 3.10(a) that transfer function G_a (s) has a very high gain at the resonant frequency, so the injected grid current tracks the reference grid current even for small values of steady-state error.

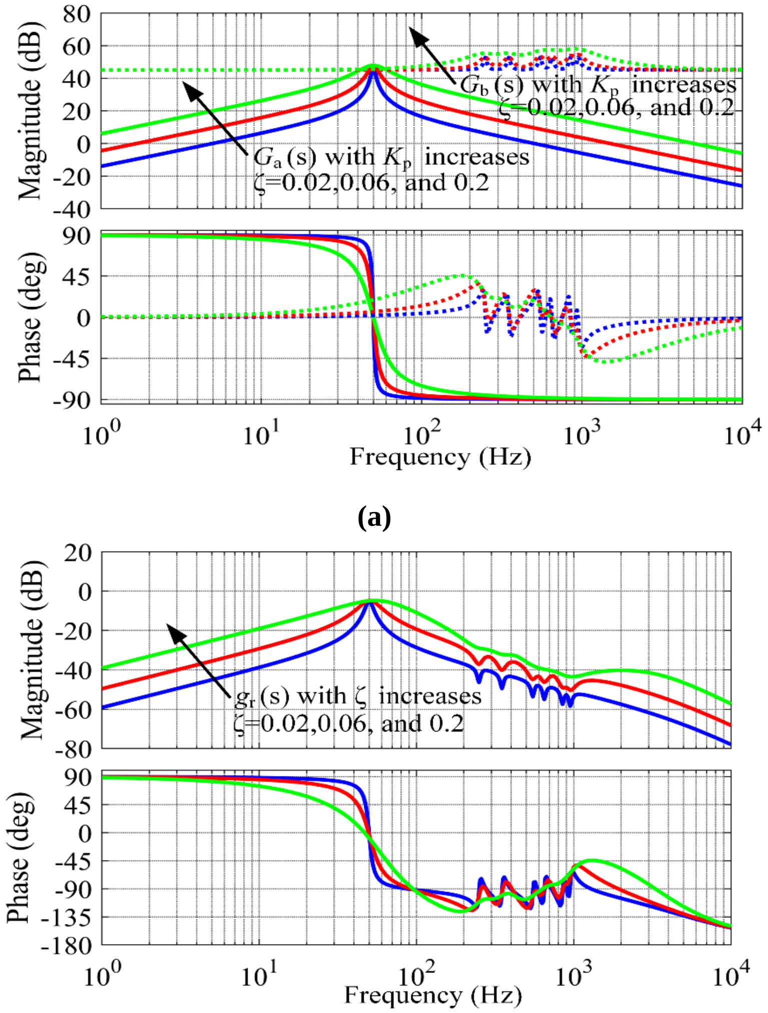

(a)

(b)

Fig. 3.9. Bode diagrams of **(a)** G_a(s) and G_b(s) **(b)** closed loop transfer functions g_r(s) with different ξ values (K_p = 30, K_r =250).

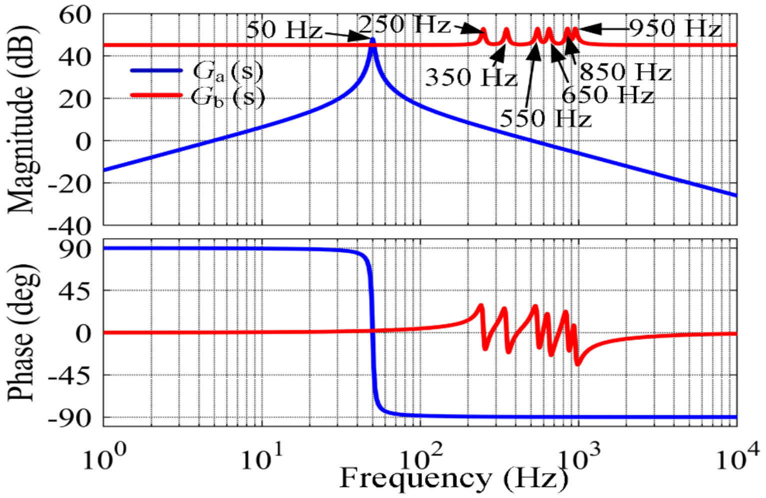

(a)

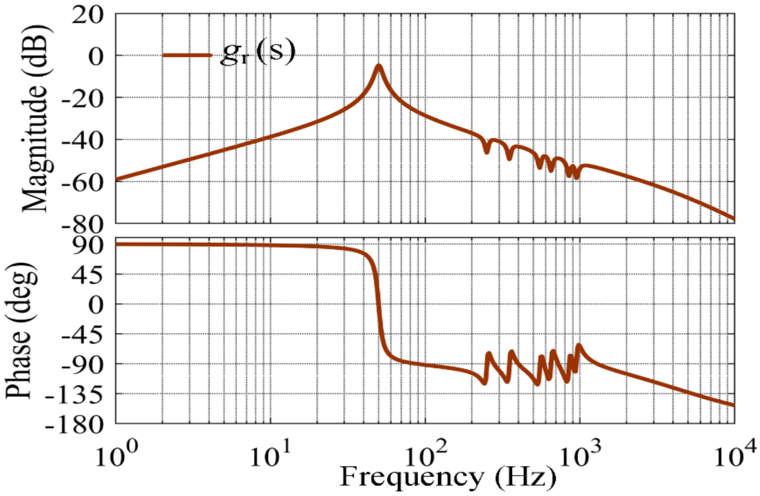

(b)

Fig. 3.10. Bode diagrams of **(a)** G_a (s) and G_b(s) **(b)** closed-loop transfer functions g_r (s) (K_p = 30, K_r = 250 and ξ=0.02).

Furthermore, it can be observed from Fig. 3.10(a) that the magnitude of the transfer function G_b(s) has peak values at 250 Hz, 350 Hz, 550 Hz, 650 Hz, 850 Hz, and 950 Hz for the selected harmonic orders 5th,7th,11th,13th,17th, and 19th. Since the output of G_b(s) is subtracted from the output of G_a (s) as shown in Fig.3.6(a), the APMR removes the selected harmonics from the output of G_a(s). The bode diagram of g_r(s) as shown in Fig. 3.10(b) shows that the magnitude at selective harmonic frequencies 250 Hz, 350 Hz, 550 Hz, 650 Hz, 850 Hz, and 950 Hz are reduced and far below than that of the fundamental resonant frequency component. However, it can be observed from Fig. 3.10 (a) that at the fundamental frequency (50 Hz), the gain of the closed-loop transfer function g_r(s) is slightly less than 0 dB (unity). Therefore, the fundamental grid current slightly reduces, when the proposed APMR controller comes into action. It is seen from Fig. 3.10(b) that a relative phase change of 90° occurs at the selected harmonic frequencies, which deteriorates the transient response of the system.

3.3.3 Compensator for Grid Voltage Sag with APMR Controller

Synchronization plays an essential role in the control of the grid-tied PV system. A good synchronization system should respond fast and accurately to grid disturbance effects, such as voltage drop, phase jump, frequency jump, and harmonic injection. Generally, the grid voltage synchronization is commonly executed through a synchronous reference frame phase-locked loop (SRF-PLL). However, under unbalanced grid voltage sag and distorted grid voltages conditions the SRF-PLL cannot effectively estimate the grid voltage's fundamental positive sequence component [114]. Therefore, the estimated *dq* components of the grid voltage contains significant ripples of 2ω (twice the grid frequency). These *dq* components are processed in the current controller for controlling the active and reactive power and thereby regulates the DC-link voltage controller for controlling the PV voltage. Consequently, significant ripples 2ω are reflected in grid injected active and reactive powers. A compensator for grid voltage sag (CGVS) in coordination with APMR controller is implemented using the PLL block to eliminate active and reactive power ripples. It reduces the ripples in the *dq* component of grid voltages, which is subsequently reflected as elimination of power ripples from the grid.

As the voltage sag occurs in the grid-tied PV system, the three-phase grid voltages are expressed as

$$\begin{bmatrix} v_{\mathrm{ga}} \\ v_{\mathrm{gb}} \\ v_{\mathrm{gc}} \end{bmatrix} = \begin{bmatrix} v_{\mathrm{ga}}^{+} \\ v_{\mathrm{gb}}^{+} \\ v_{\mathrm{gc}}^{+} \end{bmatrix} + \begin{bmatrix} v_{\mathrm{ga}}^{-} \\ v_{\mathrm{gb}}^{-} \\ v_{\mathrm{gc}}^{-} \end{bmatrix} = \begin{bmatrix} V_{\mathrm{p}}\sin(\omega t+\delta_p)+V_{\mathrm{n}}\sin(\omega t+\delta_n) \\ V_{\mathrm{p}}\sin(\omega t+\delta_p-120)+V_{\mathrm{n}}\sin(\omega t+\delta_n-120) \\ V_{\mathrm{p}}\sin(\omega t+\delta_p+120)+V_{\mathrm{n}}\sin(\omega t+\delta_n+120) \end{bmatrix} \tag{3.23}$$

By using Clark's transformation, the grid voltage v_{gabc} in (3.23) can be transferred to $v_{\mathrm{g}\alpha}$ and $v_{\mathrm{g}\beta}$ as follows

$$\begin{gathered} \begin{bmatrix} v_{\mathrm{g}\alpha} \\ v_{\mathrm{g}\beta} \end{bmatrix} = \frac{2}{3}\begin{bmatrix} 1 & -\frac{1}{2} & -\frac{1}{2} \\ 0 & \frac{\sqrt{3}}{2} & -\frac{\sqrt{3}}{2} \end{bmatrix}\begin{bmatrix} v_{\mathrm{ga}} \\ v_{\mathrm{gb}} \\ v_{\mathrm{gc}} \end{bmatrix} = \begin{bmatrix} v_{\mathrm{g}\alpha}^{+} \\ v_{\mathrm{g}\beta}^{+} \end{bmatrix} + \begin{bmatrix} v_{\mathrm{g}\alpha}^{-} \\ v_{\mathrm{g}\beta}^{-} \end{bmatrix} \\ \begin{bmatrix} v_{\mathrm{g}\alpha}^{+} \\ v_{\mathrm{g}\beta}^{+} \end{bmatrix} = \begin{bmatrix} V_{\mathrm{p}}\sin(\omega t+\delta_p) \\ -V_{\mathrm{p}}\cos(\omega t+\delta_p) \end{bmatrix} \qquad \begin{bmatrix} v_{\mathrm{g}\alpha}^{-} \\ v_{\mathrm{g}\beta}^{-} \end{bmatrix} = \begin{bmatrix} V_{\mathrm{n}}\sin(\omega t+\delta_n) \\ V_{\mathrm{n}}\cos(\omega t+\delta_n) \end{bmatrix} \end{gathered} \tag{3.24}$$

where V_{p} and V_{n} represent the positive and negative sequence voltage magnitudes; δ_{p} and δ_{n} represent the positive and negative sequence phase angles; ω represent the angular frequency. $v_{\mathrm{g}\alpha}^{+}$, $v_{\mathrm{g}\alpha}^{-}$, $v_{\mathrm{g}\beta}^{+}$ and $v_{\mathrm{g}\beta}^{-}$ are the positive and negative sequence components of $v_{\mathrm{g}\alpha}$ and $v_{\mathrm{g}\beta}$ in $\alpha\beta$ reference frame. Using Park's transformation, the voltages $v_{\mathrm{g}\alpha}$ and $v_{\mathrm{g}\beta}$ in (3.24) can be transformed to v_{gd} and v_{gq} in *dq* reference frame as follows

$$\left.\begin{gathered} \begin{bmatrix} v_{\mathrm{gd}} \\ v_{\mathrm{gq}} \end{bmatrix} = \begin{bmatrix} \sin(\omega t) & \cos(\omega t) \\ \cos(\omega t) & -\sin(\omega t) \end{bmatrix}\begin{bmatrix} v_{\mathrm{g}\alpha} \\ v_{\mathrm{g}\beta} \end{bmatrix} = \begin{bmatrix} v_{\mathrm{gd}}^{+} \\ v_{\mathrm{gq}}^{+} \end{bmatrix} + \begin{bmatrix} v_{\mathrm{gd}}^{-} \\ v_{\mathrm{gq}}^{-} \end{bmatrix} \\ \begin{bmatrix} v_{\mathrm{gd}}^{+} \\ v_{\mathrm{gq}}^{+} \end{bmatrix} = \begin{bmatrix} \sin(\omega t) & \cos(\omega t) \\ \cos(\omega t) & -\sin(\omega t) \end{bmatrix}\begin{bmatrix} v_{\mathrm{g}\alpha}^{+} \\ v_{\mathrm{g}\beta}^{+} \end{bmatrix} = \begin{bmatrix} -V_{\mathrm{p}}\cos(2\omega t+\delta_p) \\ V_{\mathrm{p}}\sin(2\omega t+\delta_p) \end{bmatrix} \\ \begin{bmatrix} v_{\mathrm{gd}}^{-} \\ v_{\mathrm{gq}}^{-} \end{bmatrix} = \begin{bmatrix} -\sin(\omega t) & \cos(\omega t) \\ \cos(\omega t) & \sin(\omega t) \end{bmatrix}\begin{bmatrix} v_{\mathrm{g}\alpha}^{-} \\ v_{\mathrm{g}\beta}^{-} \end{bmatrix} = \begin{bmatrix} V_{\mathrm{n}}\cos(2\omega t+\delta_n) \\ V_{\mathrm{n}}\sin(2\omega t+\delta_n) \end{bmatrix} \end{gathered}\right\} \tag{3.25}$$

where v_{gd}^{+}, v_{gd}^{-}, v_{gq}^{+} and v_{gq}^{-} are the positive and negative sequence components of v_{gd} and v_{gq} in *dq* reference frame.

The instantaneous active and reactive powers delivered to the grid under unbalanced grid voltage is expressed as

$$\left.\begin{aligned} P(t) &= P_0 + P_{\mathrm{c2}}\cos(2\omega t) + P_{\mathrm{s2}}\sin(2\omega t) \\ Q(t) &= Q_0 + Q_{\mathrm{c2}}\cos(2\omega t) + Q_{\mathrm{s2}}\sin(2\omega t) \end{aligned}\right\} \tag{3.26}$$

where

$$\left.\begin{aligned} P_0 &= 1.5\,(v_{\mathrm{gd}}^{+} i_{\mathrm{gd}}^{+} + v_{\mathrm{gq}}^{+} i_{\mathrm{gq}}^{+} + v_{\mathrm{gd}}^{-} i_{\mathrm{gd}}^{-} + v_{\mathrm{gq}}^{-} i_{\mathrm{gq}}^{-}) \\ P_{c2} &= 1.5\,(v_{\mathrm{gd}}^{+} i_{\mathrm{gd}}^{-} + v_{\mathrm{gq}}^{+} i_{\mathrm{gq}}^{-} + v_{\mathrm{gd}}^{-} i_{\mathrm{gd}}^{+} + v_{\mathrm{gq}}^{-} i_{\mathrm{gq}}^{+}) \\ P_{\mathrm{s2}} &= 1.5\,(v_{\mathrm{gq}}^{-} i_{\mathrm{gd}}^{+} - v_{\mathrm{gd}}^{-} i_{\mathrm{gq}}^{+} - v_{\mathrm{gq}}^{+} i_{\mathrm{gd}}^{-} + v_{\mathrm{gd}}^{+} i_{\mathrm{gq}}^{-}) \\ Q_0 &= 1.5\,(v_{\mathrm{gq}}^{+} i_{\mathrm{gd}}^{+} - v_{\mathrm{gd}}^{+} i_{\mathrm{gq}}^{+} + v_{\mathrm{gq}}^{-} i_{\mathrm{gd}}^{-} - v_{\mathrm{gd}}^{-} i_{\mathrm{gq}}^{-}) \\ Q_{\mathrm{c2}} &= 1.5\,(v_{\mathrm{gq}}^{+} i_{\mathrm{gd}}^{-} - v_{\mathrm{gd}}^{+} i_{\mathrm{gq}}^{-} + v_{\mathrm{gq}}^{-} i_{\mathrm{gd}}^{+} - v_{\mathrm{gd}}^{-} i_{\mathrm{gq}}^{+}) \\ Q_{\mathrm{s2}} &= 1.5\,(v_{\mathrm{gd}}^{+} i_{\mathrm{gd}}^{-} + v_{\mathrm{gq}}^{+} i_{\mathrm{gq}}^{-} - v_{\mathrm{gd}}^{-} i_{\mathrm{gd}}^{+} - v_{\mathrm{gq}}^{-} i_{\mathrm{gq}}^{+}) \end{aligned}\right\} \tag{3.27}$$

where i^{+}_{gd}, i^{+}_{gq}, i^{-}_{gd} and i^{-}_{gq} are the positive and negative sequence of the grid currents in *dq* reference frame.

It is noticed from (3.25) that the positive and negative sequence grid voltages (v^{+}_{gd},v^{+}_{gq},v^{-}_{gd} and v^{-}_{gq}) contain twice the grid frequency ripples. This grid frequency ripples (2ω) are reflected in the DC-link voltage. Due to this grid frequency ripples, the active and reactive power oscillates at twice the grid frequency. These oscillations are induced by the negative sequence grid voltages, which is also reflected in the *dq* component. The CGVS is developed by including a band-reject filter with a cut-off frequency of (2ω), and is integrated with the SRF-PLL control loop to filter the ripples in *dq* components as shown in Fig. 3.11.

The transfer function of a band-reject filter is expressed as [116]

$$\mathrm{G}_{\mathrm{brf}}(s) = \frac{s^2 + \omega_n{}^2}{s^2 + 2\alpha\omega_n s + \omega_n{}^2} \tag{3.28}$$

where ω_{n} and $\alpha\omega_{\mathrm{n}}$ are the band-reject and cut-off frequencies of the band-reject filter.

To filter out the 2ω ripples, the *d* and *q* axes grid voltages are passed through CGVS. By doing so, the twice the grid frequency ripples (2ω) in the positive and negative sequence grid voltages (v^{+}_{gd}, v^{+}_{gq}, v^{-}_{gd} and v^{-}_{gq}) are eliminated by canceling the terms cos (2ωt+ δ_{p}), sin (2ωt+ δ_{p}), cos (2ωt+ δ_{n}) and sin (2ωt+δ_{n}) in the expression given in (3.25). Furthermore, with voltage ripples eliminations, the CGVS eliminates the oscillations of active and reactive power introduced by the oscillating components (P_{c2}, P_{s2}, Q_{c2} and Q_{s2}).

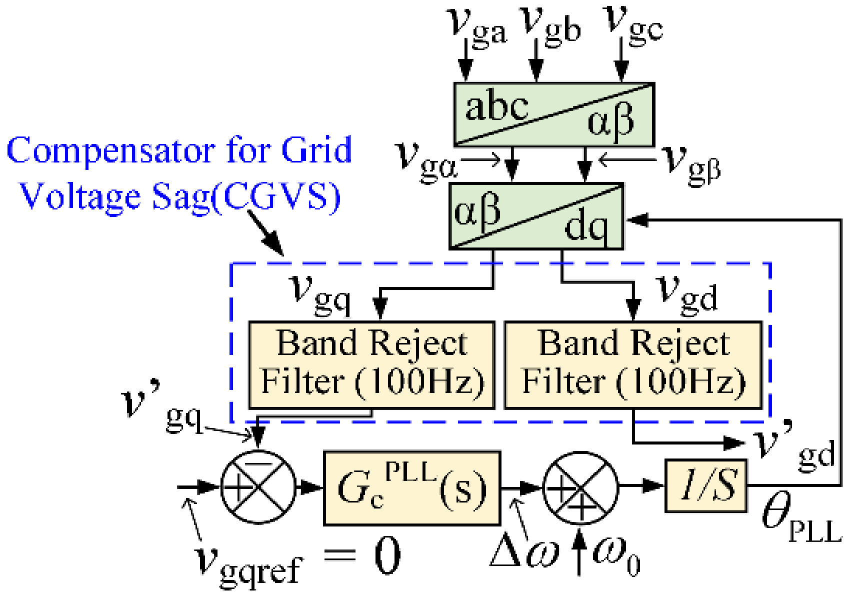

Fig. 3.11. Block diagram of PLL with CGVS.

3.4 Experimental Verifications

To validate the effectiveness of the proposed control strategy for the grid-tied PV system, a set of experimental tests have been carried out with the laboratory prototype of 3.8 kW as shown in Fig. 3.12. The detailed system parameters of the grid-tied PV system used in the experiment are listed in Table 3.1. The grid voltage is generated by a three-phase grid simulator ITEC GS010 415-16. The solar power generation is emulated using a programmable solar PV simulator Chroma 62100H-600S. The prototype consists of a SEMIKRON SM150GB 12T4 power module, including six insulated gate bipolar transistors (IGBTs) and gate drivers with a protection circuit. The proposed control strategy is executed under the hardware in the loop (HIL) environment of a real-time digital simulator OPAL-RT OP4510. The performance of the proposed control strategy is compared with the conventional PMR controller. The following cases are considered to verify the proposed control strategy.

3.4.1 Performance Evaluation of Proposed APMR Controller Under Harmonic Disturbances

The performance of the grid-tied PV system under harmonic grid voltage disturbances are investigated in this section. To verify the feasibility of the proposed control strategy, the PV unit is connected to a grid with harmonically distorted grid voltage. In this case, the harmonically distorted grid voltages are generated by injecting the harmonic components: 5th harmonic -12%, 7th harmonic -12%, 11th harmonic -10%, 13th harmonic -10%, 17th harmonic - 6%, and 19th harmonic - 6%. The experimental waveforms of grid voltage and grid current without compensation using PI controller, with the proposed APMR controller and the conventional PMR controller under the dynamic conditions are captured and shown in Fig. 3.13. It can be noticed from Fig.3.13 that the grid current is severely distorted without harmonic compensation using PI controller. When the current controller is activated, the grid currents are less distorted and regulated to be more sinusoidal and balanced with the proposed APMR controller than the conventional PMR controller. The proposed APMR controller can effectively reduce the grid current distortions with enhanced current quality. The grid current's Fast Fourier Transform (FFT) spectrum using the proposed APMR and conventional PMR control strategies are in Fig. 3.14. It can be observed that the %THD of the grid current without compensation using the conventional PI controller is 8.88%. However, the harmonic compensation with the APMR and conventional PMR controllers, the THD becomes 3.6 % and 7.47%, respectively. The THD grid current with the proposed APMR controller is within 5%, which satisfies the IEEE 1547 standards [117]. Thus, it is concluded that the harmonic rejection capability of the proposed APMR controller is superior and more effective over the conventional PMR controller in the presence of distorted grid voltages.

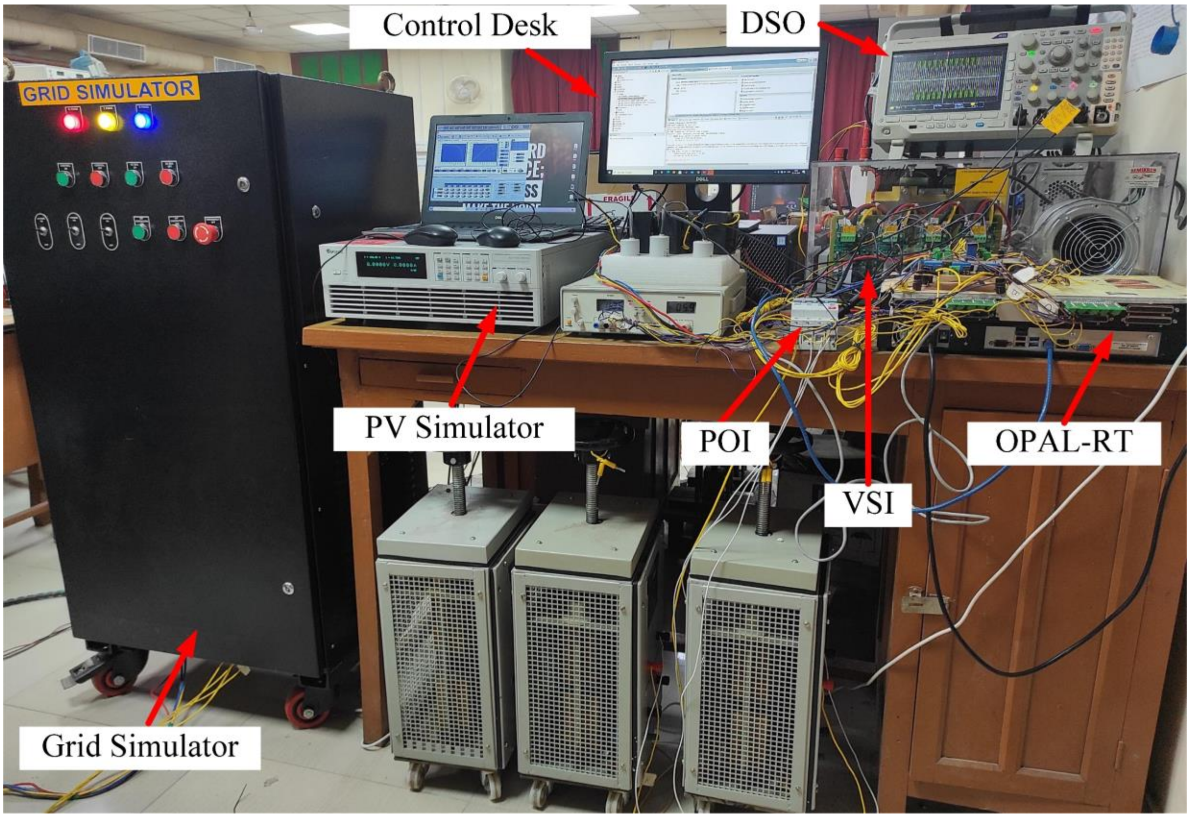

Fig. 3.12. Photograph of laboratory setup.

Table 3.1. Real time system and control parameters

	Description	Symbol	Value
System Parameters	Grid Voltage Amplitude	V_g	110 V (L-L rms)
	Grid frequency	f_g	50 Hz
	Switching frequency	f_{sw}	10 kHz
	Grid inductance	L_g	.5 mH
	Inverter side inductance	L_{if}	5 mH
	Filter capacitance	C_f	10 µF
	Grid side inductance	L_{of}	0.8 mH
	DC link capacitance	C_{dc}	4700 µF
	PV open circuit voltage	V_{PVoc}	450 V
	PV short circuit current	I_{PVsc}	10.46 A
	PV MPP voltage	V_{MPP}	390 V
	PV MPP current	I_{MPP}	9.76 A
	PV Maximum power	P_{MPP}	3.8 kW
Control Parameters	PI controller (DC-link voltage controller)	K_{pvdc}, K_{ivdc}	3,65
	APMR controller	K_p, K_r, K_{rh}, ξ	30, 250,250,0.02

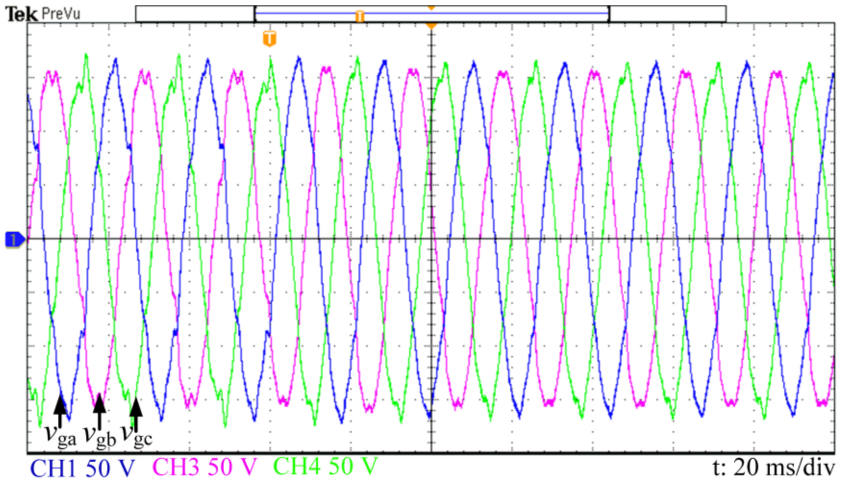

(a)

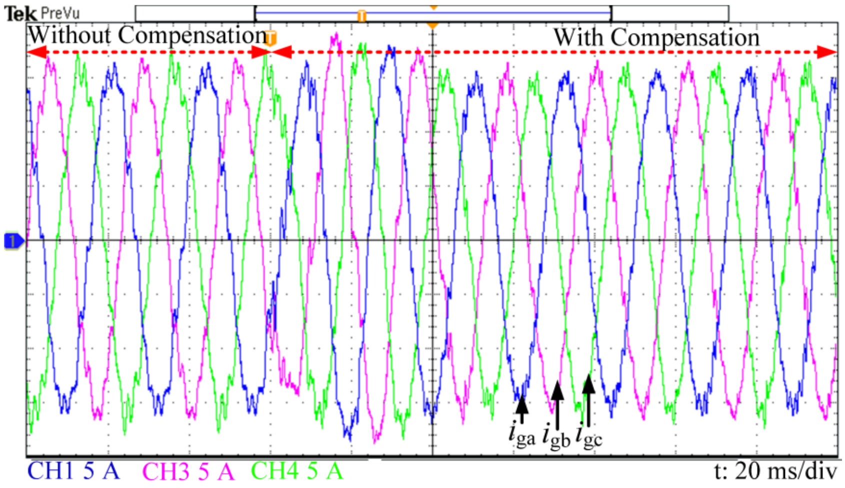

(b)

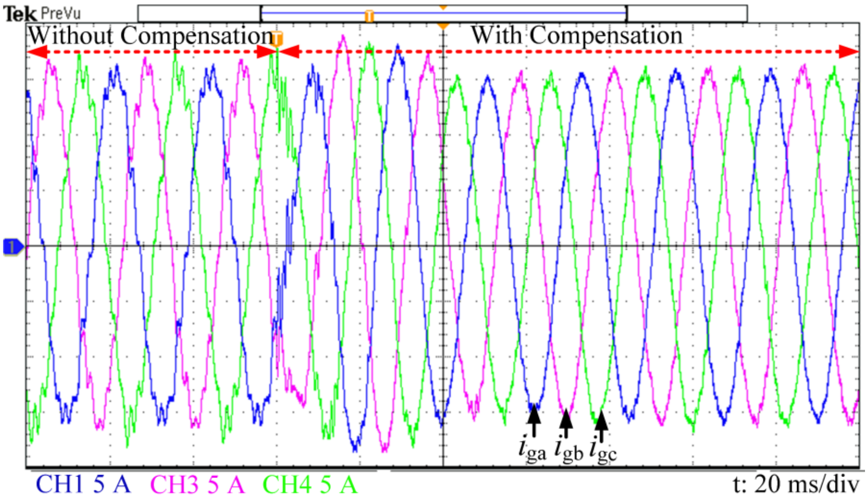

(c)

Fig. 3.13. Real-time experimental waveforms of **(a)** grid voltage (**b**)-(**c**) grid current without compensation using PI controller, with the conventional PMR controller and with the proposed APMR controller.

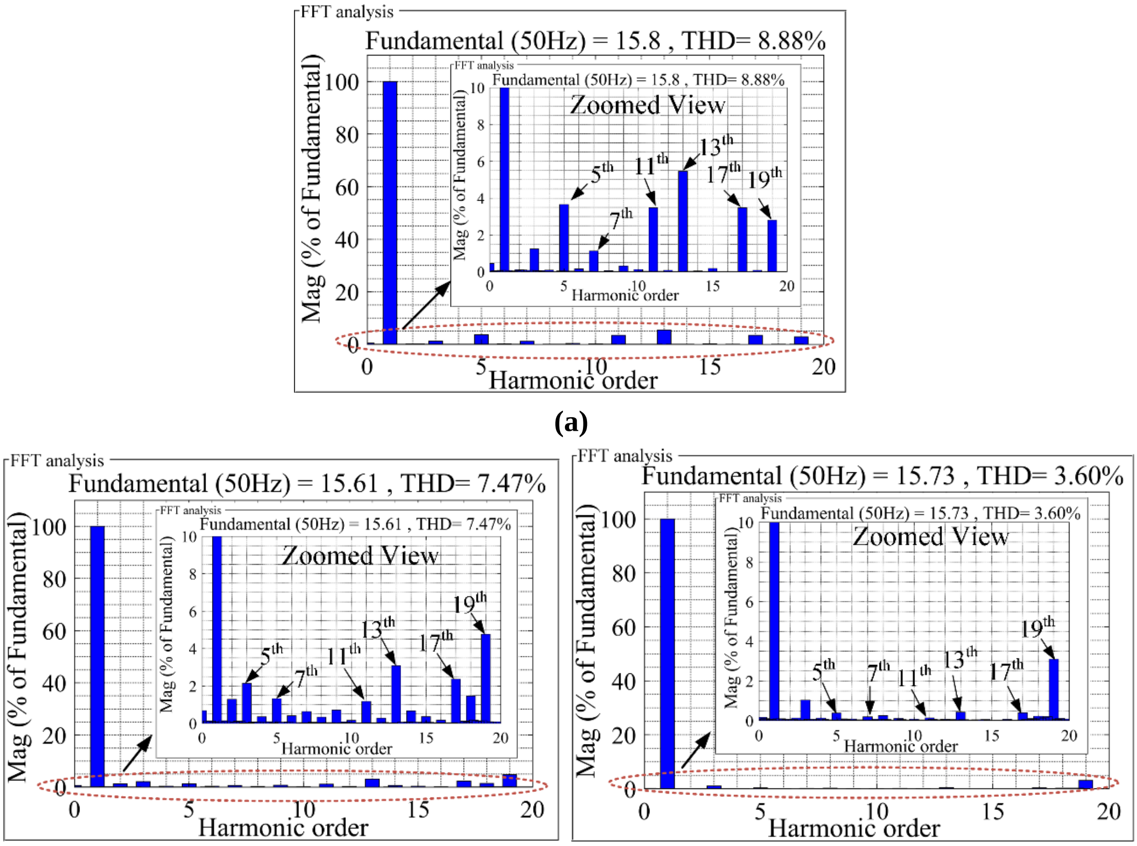

(a)

(b) (c)

Fig. 3.14. FFT spectra the grid current with different control strategies **(a)** without compensation using PI controller **(b)** with the conventional PMR controller **(c)** with the proposed APMR controller.

3.4.2 Performance Evaluation of Proposed APMR Controller During Grid Frequency Variation

This section discusses the effectiveness of the proposed APMR controller during grid frequency variations. During grid frequency variations from 50 Hz to 52 Hz, the waveforms of the grid-tied PV system for the proposed APMR controller and CPMR controller are shown in Fig. 3.15. It is observed from Fig. 3.15 (a)-(b) that the grid frequency with the proposed APMR controller stabilizes quickly with settling time of 60 ms, however with the CPMR controller, the settling time is 120 ms. It can be noticed from Figs. 3.15 (c)-(d) that power fluctuations with the APMR controller are less than the CPMR controller.

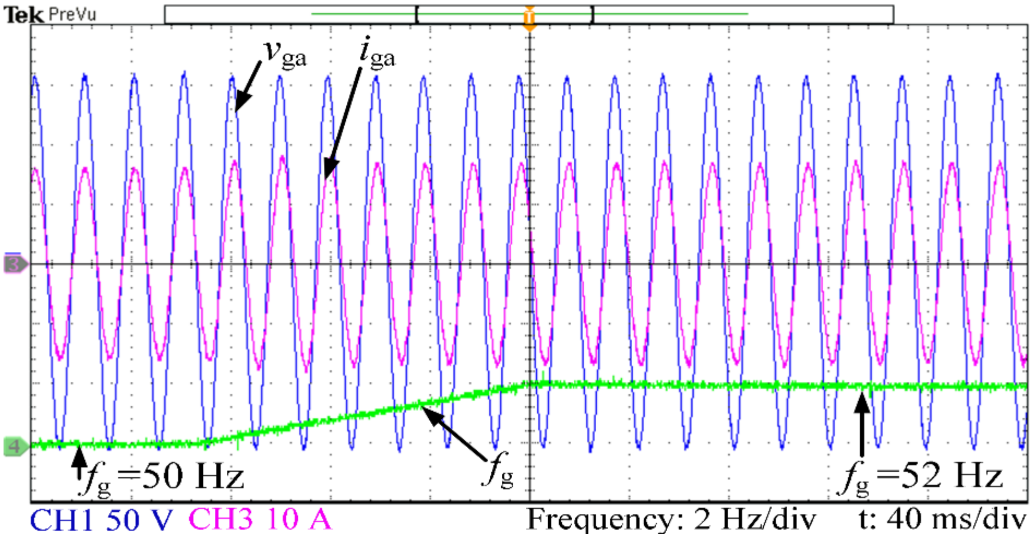

(a)

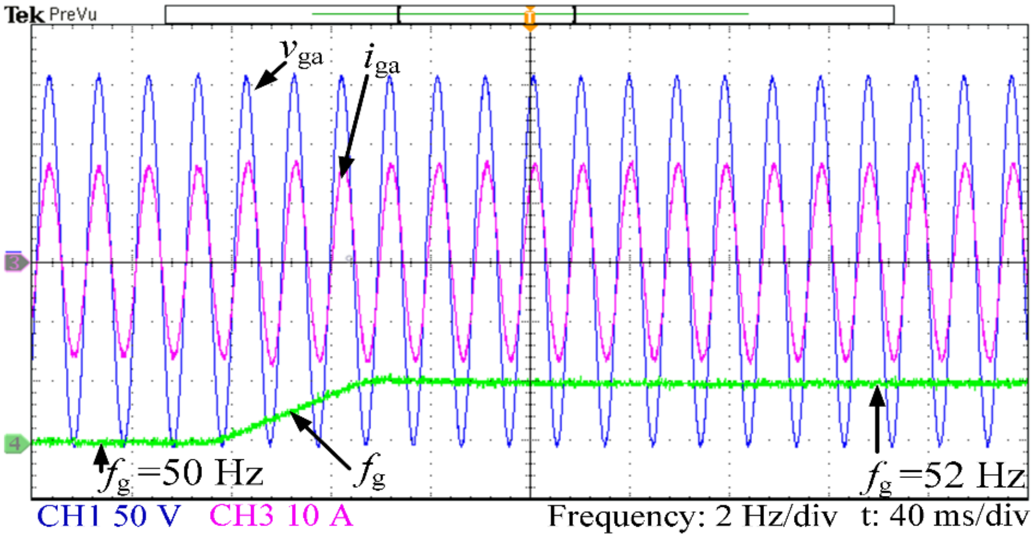

(b)

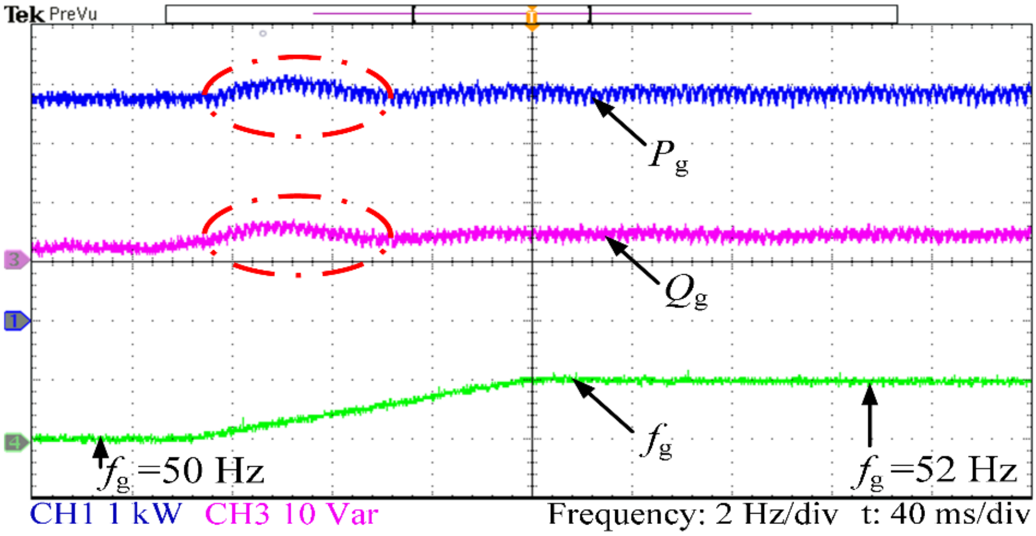

(c)

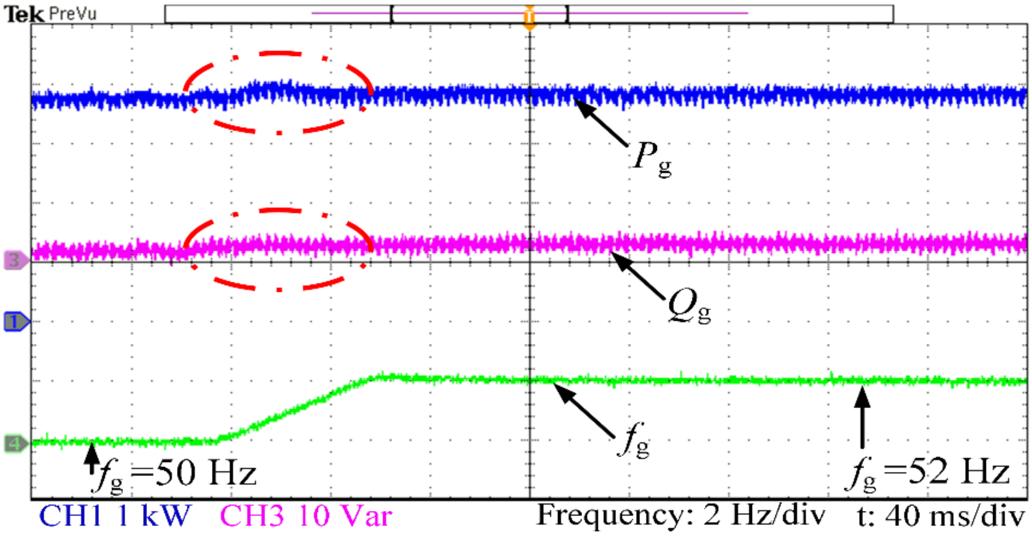

(d)

Fig.3.15. Experimental waveforms of the grid voltage (v_g), grid current (i_g), grid injected active power (P_g), grid injected reactive power (Q_g)and grid frequency (f_g) when grid frequency changes from 50 Hz to 52 Hz. **(a), (c)** with the CPMR controller **(b), (d)** with the proposed APMR controller.

Moreover, the effectiveness of the proposed APMR controller to enhance the frequency adaptability for a frequency variation (decrease in frequency from 52 to 50 Hz) is shown in Fig. 3.16. It can be observed that the APMR controller has a faster settling time with negligible active and reactive power oscillations. Therefore, it is concluded that the proposed APMR controller's frequency adaptability is superior as compared to the CPMR controller during grid frequency variations.

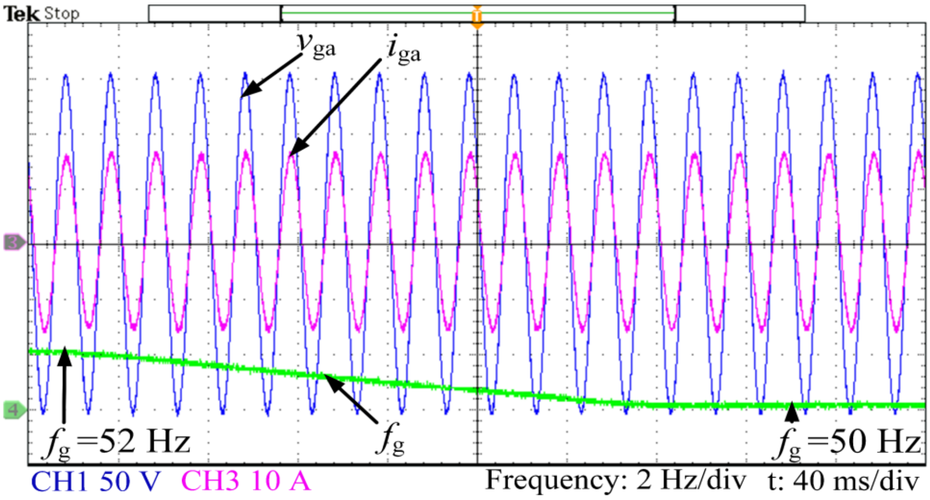
Tek Stop
v_{ga}
i_{ga}
f_g=52 Hz
f_g
f_g=50 Hz
CH1 50 V
CH3 10 A
Frequency: 2 Hz/div
t: 40 ms/div

(a)

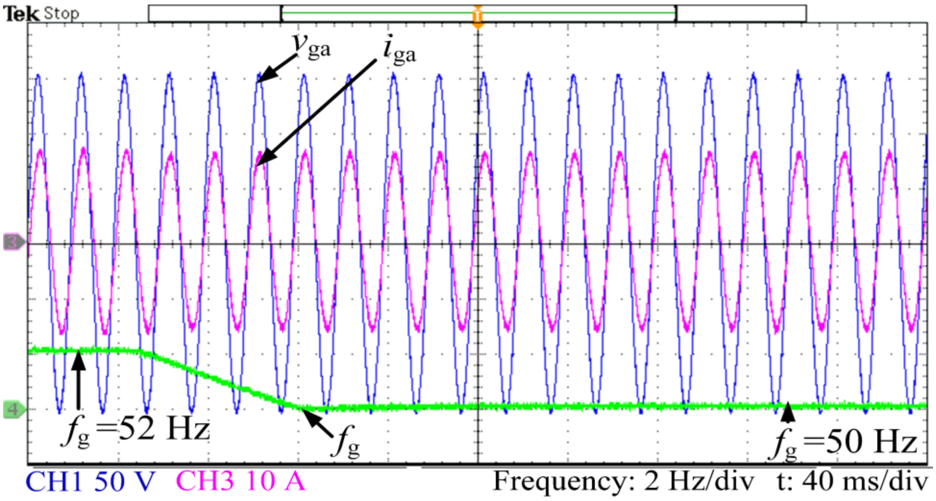
Tek Stop
v_{ga}
i_{ga}
f_g=52 Hz
f_g
f_g=50 Hz
CH1 50 V
CH3 10 A
Frequency: 2 Hz/div
t: 40 ms/div

(b)

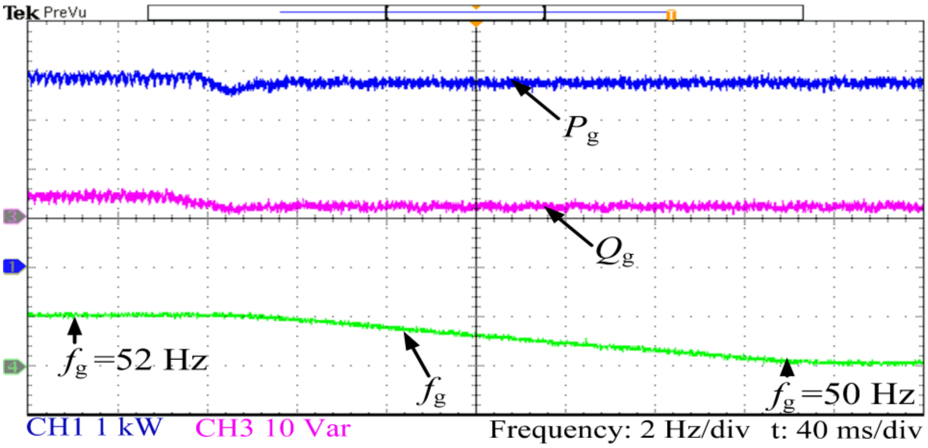
Tek PreVu
P_g
Q_g
f_g=52 Hz
f_g
f_g=50 Hz
CH1 1 kW
CH3 10 Var
Frequency: 2 Hz/div
t: 40 ms/div

(c)

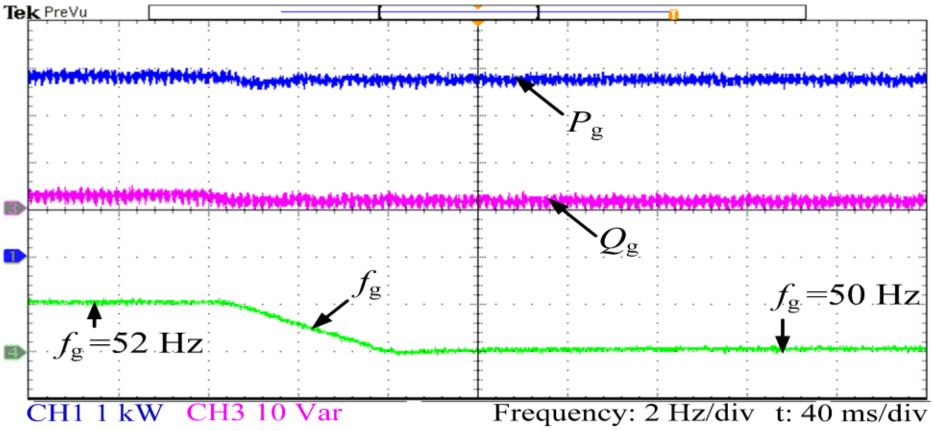

(d)

Fig. 3.16. Experimental waveforms of the grid voltage (v_g), grid current (i_g), grid injected active power (P_g), grid injected reactive power (Q_g)and grid frequency (f_g) when grid frequency changes from 52 Hz to 50 Hz. **(a), (c)** with the CPMR controller **(b), (d)** with the proposed APMR controller.

3.4.3 Performance Evaluation of Proposed APMR Controller with CGVS Under Grid Voltage Sag

The effectiveness of the proposed scheme of APMR controller with CGVS in eliminating the active power and reactive powers ripples caused by voltage sags is discussed in this section. The proposed control strategy's performance for a single-phase voltage sag with a 40% drop in phase 'a' occurred from t = 80 ms to t = 320 ms is demonstrated in Fig. 3.17 (a). It can be observed from Figs. 3.17 (b)-(c) that the current waveform obtained through CGVS with APMR is more balanced and sinusoidal than the waveform obtained through CGVS with the conventional PMR. It can be seen from Fig. 3.17 (d)-(e) that the active and reactive powers oscillate twice the grid frequency using the conventional PMR controller with CGVS. However, the proposed scheme of APMR controller with CGVS injects constant active and reactive powers to the grid and the power oscillations are eliminated.

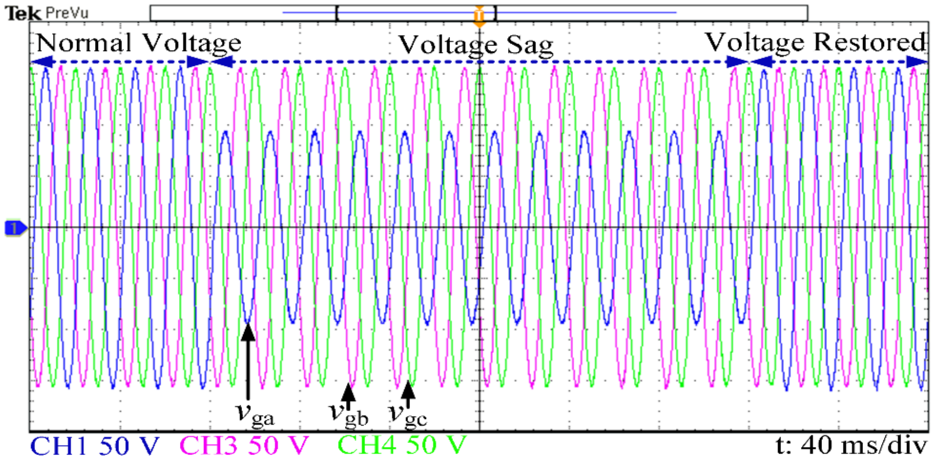

(a)

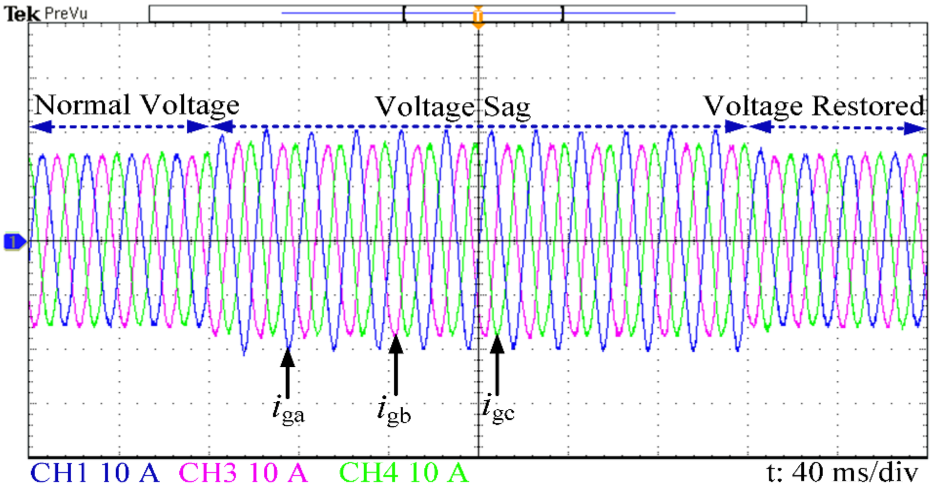
Tek PreVu
Normal Voltage
Voltage Sag
Voltage Restored
i_{ga}
i_{gb}
i_{gc}
CH1 10 A
CH3 10 A
CH4 10 A
t: 40 ms/div

(b)

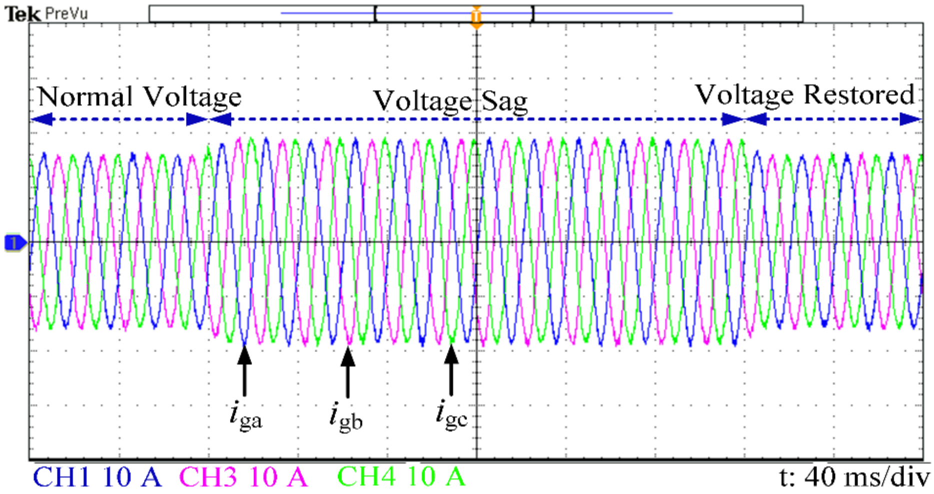
Tek PreVu
Normal Voltage
Voltage Sag
Voltage Restored
i_{ga}
i_{gb}
i_{gc}
CH1 10 A
CH3 10 A
CH4 10 A
t: 40 ms/div

(c)

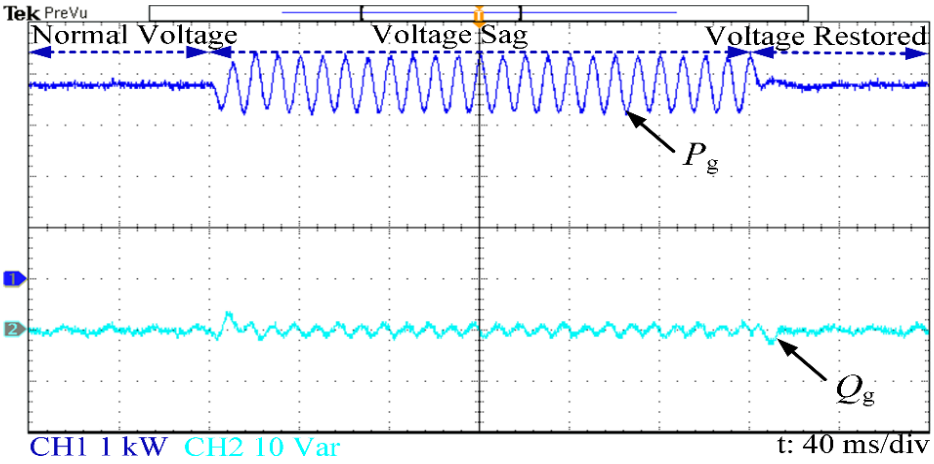
Tek PreVu
Normal Voltage
Voltage Sag
Voltage Restored
P_g
Q_g
CH1 1 kW
CH2 10 Var
t: 40 ms/div

(d)

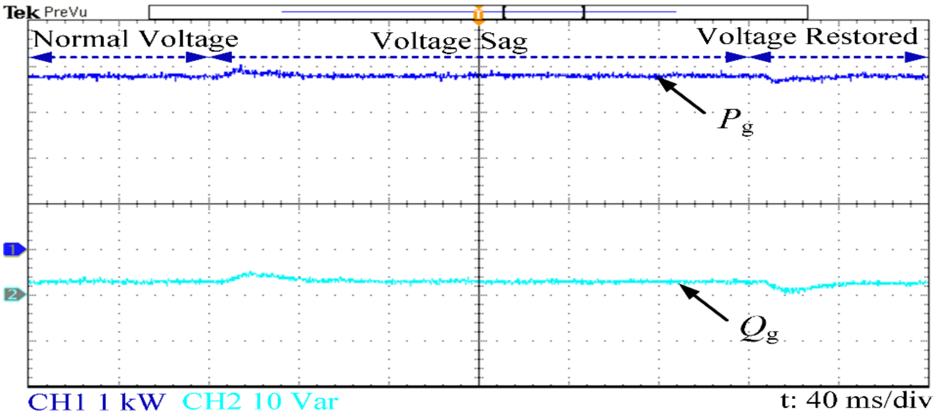

(e)

Fig. 3.17. Experimental waveforms with a 40% voltage sag in phase *a*. **(a)** grid voltages **(b)-(c)** grid current with the conventional PMR controller with CGVS, and with the proposed APMR controller with CGVS, respectively **(d)-(e)** active and reactive power with the conventional PMR controller with CGVS and with the proposed APMR controller and CGVS respectively.

Fig. 3.18 shows the real-time experimental waveforms of the grid-tied PV system for 40% voltage sag in phase a and phase *b*. The voltage sag is applied at t= 40 ms and clears at t= 140 ms. It can be observed from Fig. 3.18 that the grid current waveforms with the proposed APMR controller are more sinusoidal than the conventional PMR controller. Also, the ripples in active and reactive power are eliminated using the APMR controller. The real-time experimental waveforms of the grid-tied PV system with another case, i.e., unbalanced phase voltages ($v_{ga} = 110\angle 0°$, $v_{gb} = 55\angle{-105}°$, $v_{gc} = 66\angle 105°$) is illustrated in Fig. 3.19. The unbalance voltage occurs at $t = 80$ ms and clears at $t = 320$ ms. It is evident from Figs. 3.19 (b)-(c) that as compared with the conventional PMR controller with CGVS, the grid current waveforms obtained through the proposed APMR controller with CGVS are more sinusoidal and balanced. Also, the proposed APMR controller with CGVS eliminates active and reactive power oscillations, as shown in Fig. 3.19 (d)-(e). Thus, in such severe distorted voltage sag condition, with the proposed control strategy of APMR with CGVS, the grid current waveform is almost sinusoidal and the power ripples are also eliminated.

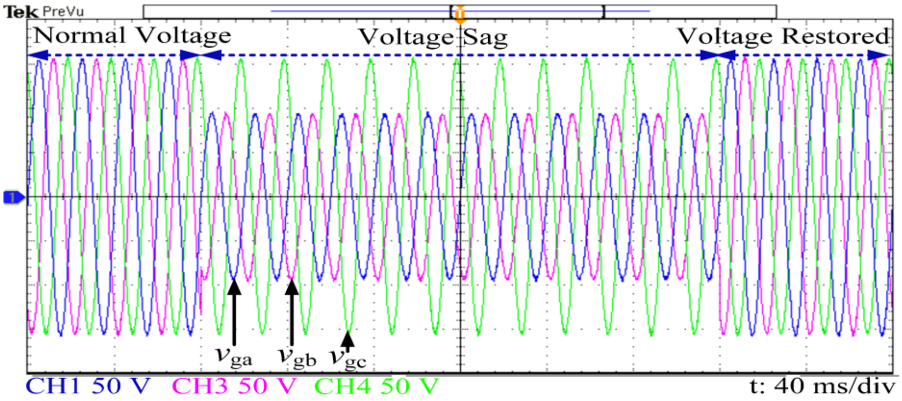

(a)

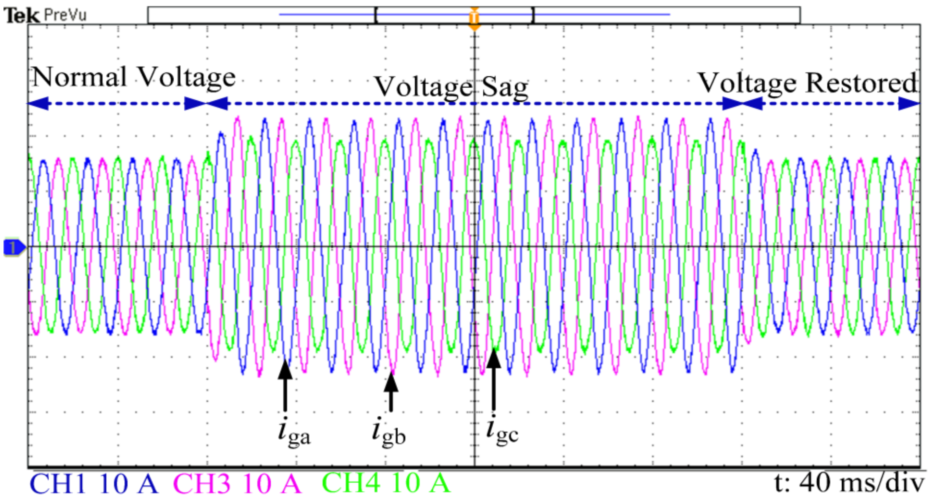
Tek PreVu
Normal Voltage
Voltage Sag
Voltage Restored
i_{ga}
i_{gb}
i_{gc}
CH1 10 A
CH3 10 A
CH4 10 A
t: 40 ms/div

(b)

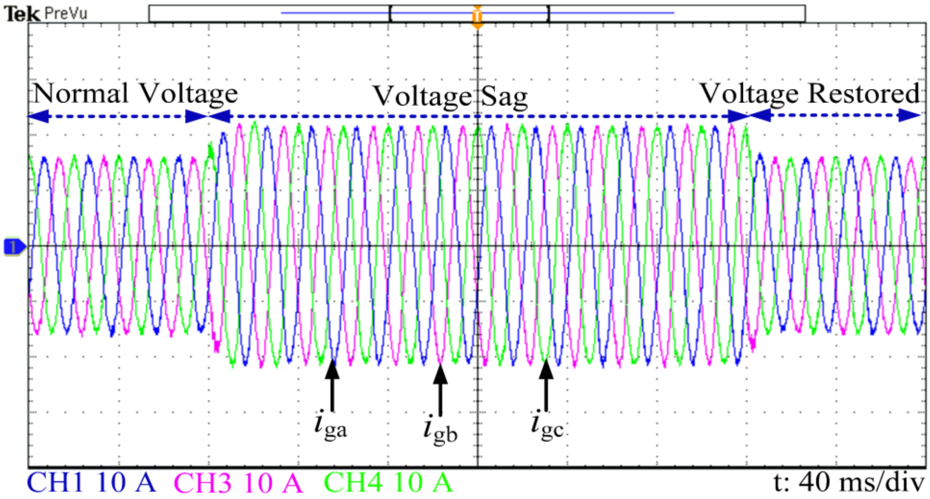
Tek PreVu
Normal Voltage
Voltage Sag
Voltage Restored
i_{ga}
i_{gb}
i_{gc}
CH1 10 A
CH3 10 A
CH4 10 A
t: 40 ms/div

(c)

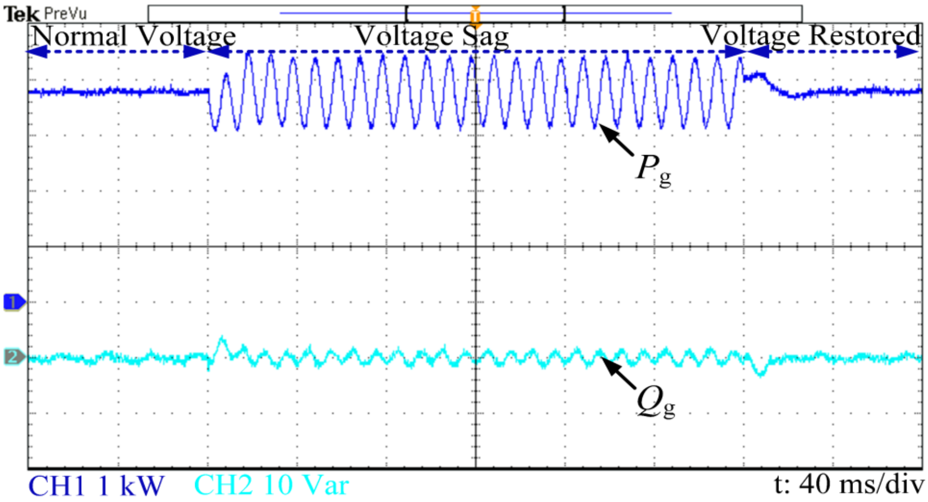
Tek PreVu
Normal Voltage
Voltage Sag
Voltage Restored
P_g
Q_g
CH1 1 kW
CH2 10 Var
t: 40 ms/div

(d)

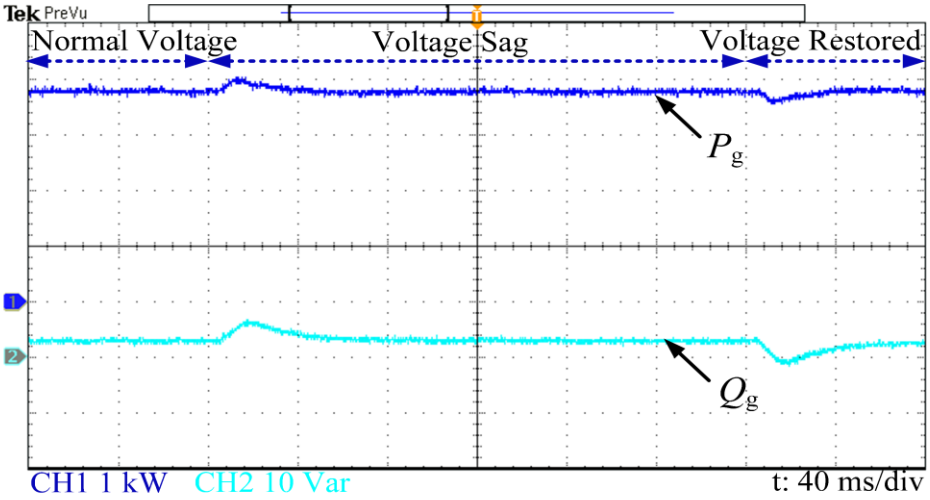

(e)

Fig. 3.18. Experimental waveforms with 40 % voltage sag in phase *a* and phase *b*. **(a)** grid voltages **(b)-(c)** grid current with the conventional PMR controller with CGVS, and with the proposed APMR controller with CGVS, respectively **(d)-(e)** active and reactive power with the conventional PMR controller with CGVS and with the proposed APMR controller and CGVS respectively.

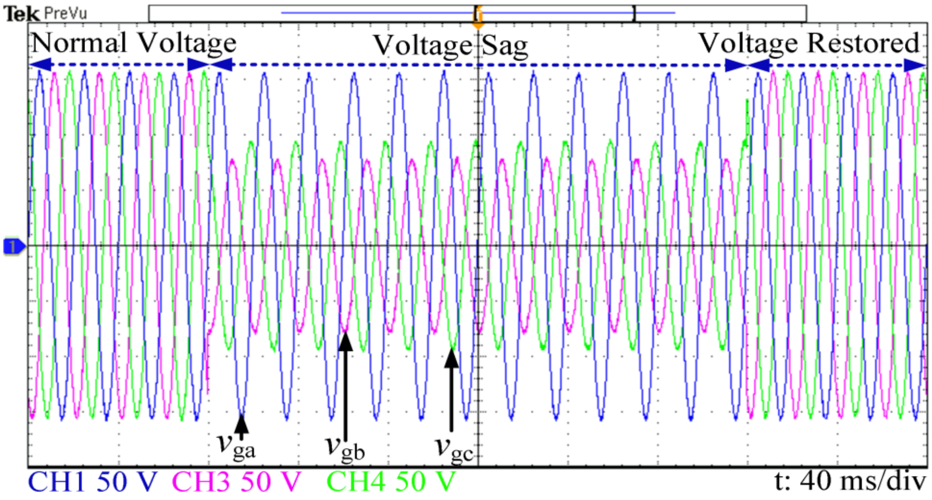

(a)

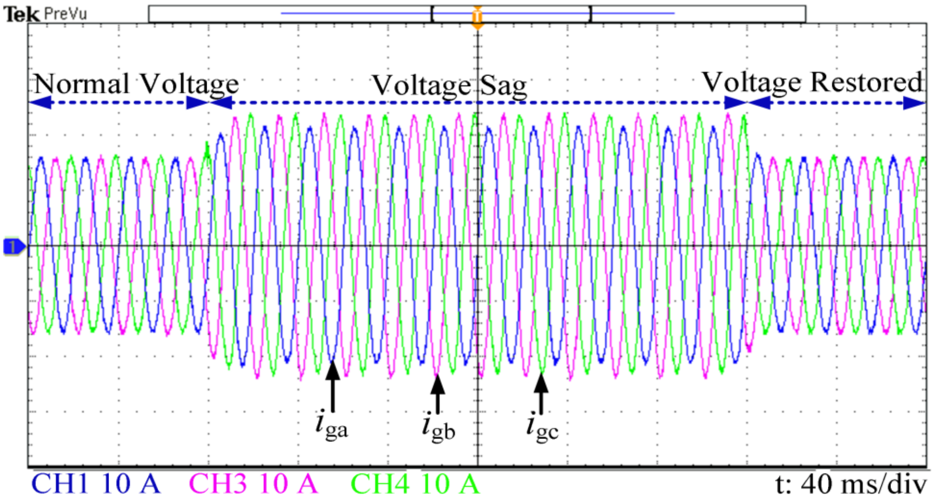

(b)

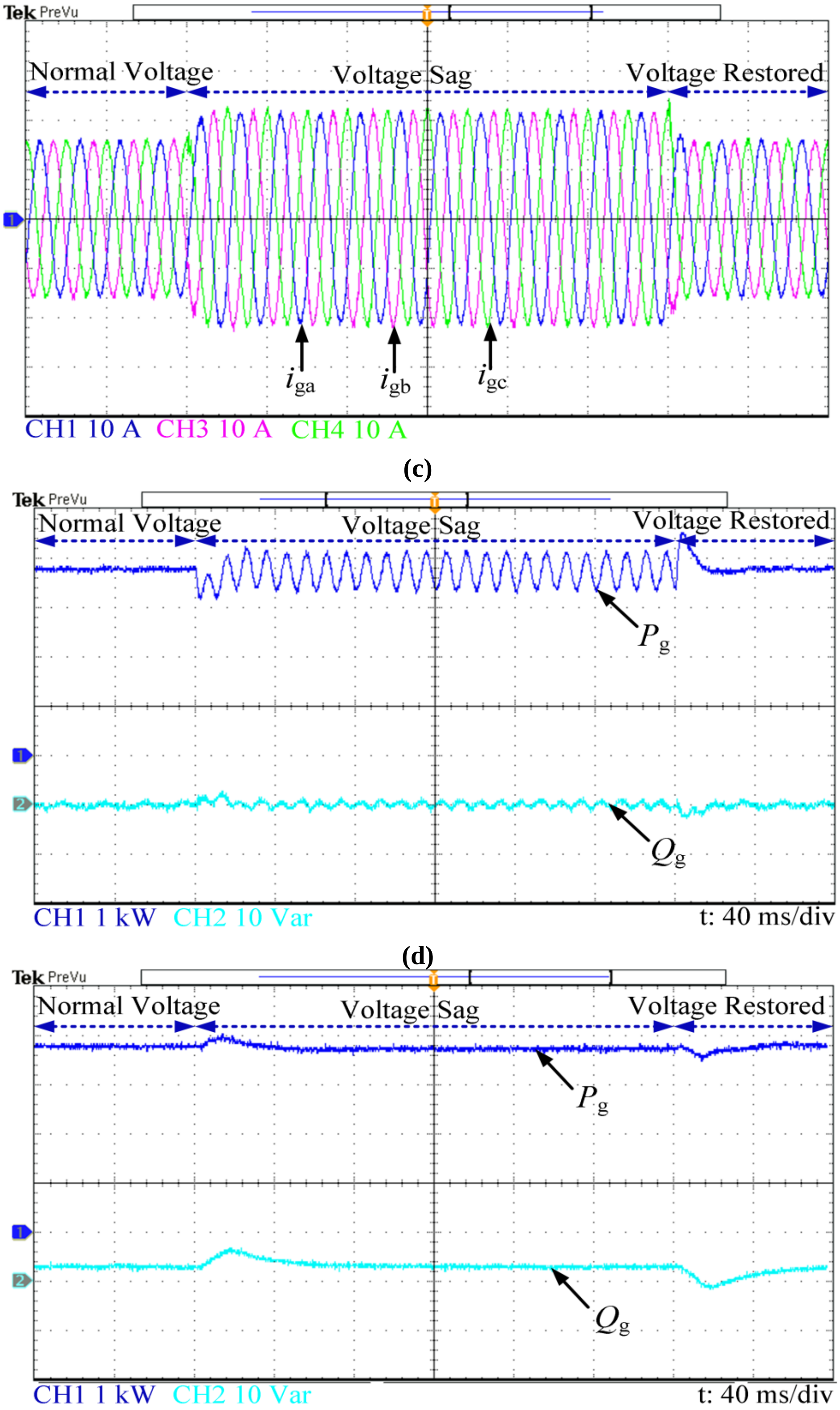

(c)

(d)

(e)

Fig. 3.19. Experimental waveforms under unbalanced grid voltage condition (v_{ga} =110∠ 0°, v_{gb} =55∠ -105°, v_{gc} =66∠ 105°) **(a)** grid voltages **(b)-(c)** grid current with the conventional PMR controller with CGVS, and proposed APMR controller with CGVS, respectively **(d)-(e)** active and reactive power with the conventional PMR controller with CGVS and with the proposed APMR controller with CGVS.

3.4.4 Tracking Performance Evaluation with Adaptive Step Size INC MPPT

The dynamic performance of the adaptive step size INC (ASINC) MPPT controller is compared with the fixed step size INC (FSINC) MPPT controller as demonstrated in Fig. 3.20. The step size Δv_{pv} of the FSINC MPPT is 5V and the scaling coefficient n of the ASINC MPPT is 0.75. Initially, at the standard atmospheric test conditions (irradiance I_{r} = 1000 W/m^2, temperature T_{m} = 25 °C) the PV voltage reference V_{PVref} and the PV power P_{PV} generated from the PV array is considered as 300 V and 3.1 kW, respectively. It can be observed from Fig. 3.20 that both the MPPT controllers start at time $t = t_1$ s. It can be noticed that the ASINC MPPT controller tracks the PV voltage and reaches the MPP point with a tracking time of $t_{\mathrm{ASINC\text{-}MPP}}$ = 1.4 s, which is faster as compared to the fixed step size INC MPPT controller with tracking time $t_{\mathrm{FSINC\text{-}MPP}}$ = 3.0 s. It can be observed that with ASINC MPPT controller near the MPP voltage ($\mathrm{V_{MPP}}$ = 390 V) has lesser oscillations around the interval (389.5-390.5 V) as compared to the fixed step size INC MPPT controller, which oscillates in the interval 384 V- 396 V. Therefore, it is concluded that the ASINC MPPT controller tracks the MPP with negligible fluctuations and precise and fast dynamic response with faster tracking time as compared to the FSINC MPPT controller. The maximum power (P_{MPP}) generated from the PV array is 3.8 kW as shown in Fig 3.20 (b). At $t = t_2$, the environmental condition is changed from (I_{r} = 1000 W/m^2, T_{m} = 25 °C) to (I_{r} = 700 W/m^2, T_{m} = 50 °C). The tracking time to reach the new MPP point with ASINC MPPT (V_{MPP} = 340 V and P_{MPP} = 3.3 kW) is $t_{\mathrm{ASINC\text{-}MPP} =}$ 1.2 s, while the tracking time with FSINC MPPT is $t_{\mathrm{FSINC\text{-}MPP}}$ = 2.7 s. Further, at $t = t_3$, the environmental conditions are changed from (I_{r} = 700 W/m^2, T_{m} = 50 °C) to (I_{r} =1000 W/m^2, T_{m} = 25°C). The ASINC and FSINC MPPT controllers track the MPP (V_{MPP} = 390, P_{MPP} = 3.8 kW) with tracking time $t_{\mathrm{ASINC\text{-}MPP}}$ = 1.4 s and $t_{\mathrm{FSINC\text{-}MPP}}$ = 2.0 s, respectively.

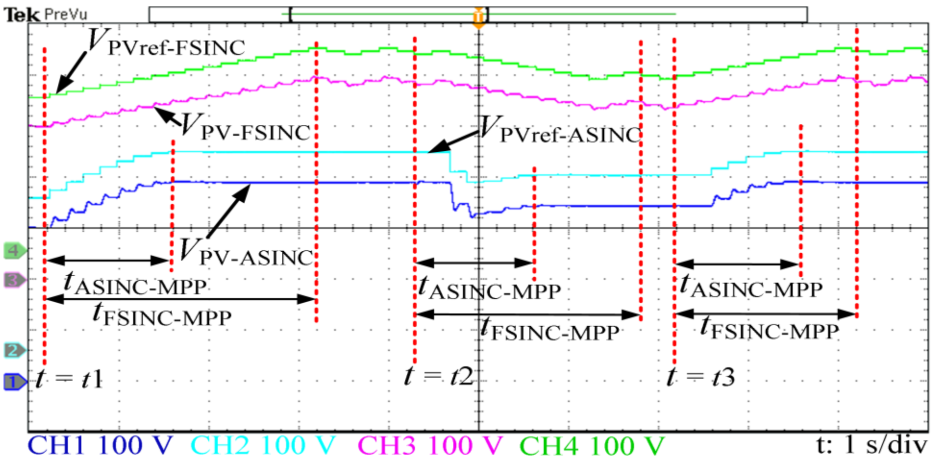

(a)

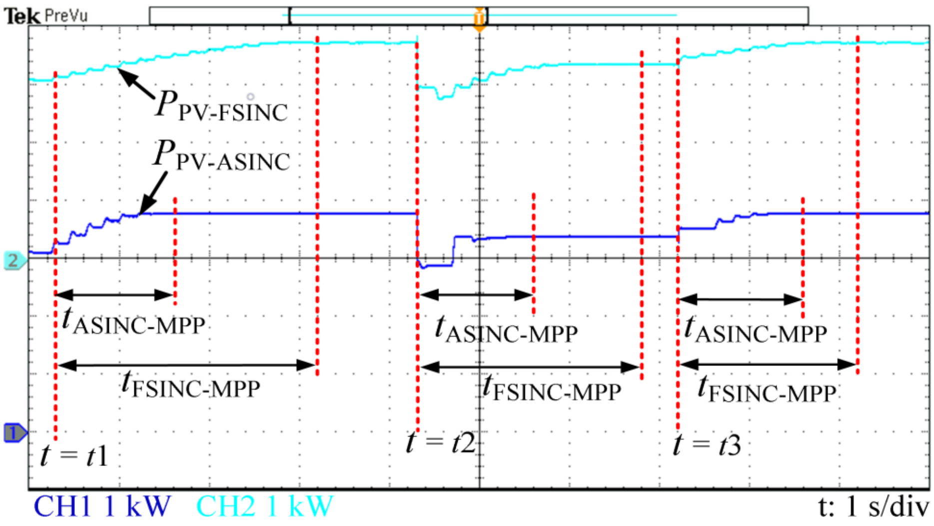

(b)

Fig. 3.20. Real-time dynamic experimental waveforms of the ASINC MPPT and FSINC MPPT controller under fast environmental changes. **(a)** PV Voltage. **(b)** PV Power.

3.4.5 Comparison Between the Proposed Control Strategy with the Existing Control Strategy

The proposed control strategy of APMR controller with CGVS has been compared with the existing control strategies, such as the conventional PMR (CPMR) controller [113], resonant current control strategy (RCC) [119] and vector current control direct power control (VCC-DPC) [120]. The main features of the proposed APMR control strategy are compared with the three control strategies qualitatively and quantitively, as shown in Table 3.2 . In CPMR and RCC, twice the grid frequency power ripples occur during the grid voltage sags. However, the proposed control strategy eliminates twice of the grid frequency power ripples. Also, as compared to CPMR, RCC and VCC- DPC the grid current harmonics are reduced and the frequency tracking ability is better with the proposed control strategy. The implementation of the proposed control strategy is simpler than CPMR and RCC. It is observed that the proposed control strategy adapts quickly settles to the new grid frequency faster (60 ms) as compared to the CPMR and RCC (120 ms). The THD of the grid current by using VCCDPC, CPMR and RCC control strategies are 8.88 %, 7.47%, and 7.47%, respectively. However, the grid current THD using the proposed control strategy is 3.6% which is lower than the other control strategies and as per the IEEE 519 standard. It is observed that with the CPMR control strategy, the peak-to-peak active power ripple during grid voltage sag is 0.8 kW which is 21% of the rated grid injected active power. However, with the proposed APMR control strategy, the active power ripple is very low 0.015 kW which is 0.43 % of the rated grid injected active power. The proposed control strategy performs satisfactorily while reducing grid current harmonics, eliminating power ripples under grid frequency variations and MPPT tracking

Table 3.2. Comparative Study of the Proposed Control Strategy With the Existing Control Strategies

Comparision Catagory	**Conventional PMR controller (CPMR) [113]**	**Resonant current control strategy (RCC) [119]**	**Vector current control direct power control (VCC-DPC) [120]**	**Proposed control strategy**
Grid current harmonics reduction ability	Medium	Medium	Medium	Better
Implementation complexity	Complicated	Moderate	Simple	Simple
Power ripples during voltage sag	High	High	Medium	Low
Frequency tracking ability	Not Reported	Not Reported	Better	Best
MPPT tracking	Not Reported	Not Reported	Not Reported	Reported
THD of grid currents	7.47 %	7.47 %	8.88 %	3.6 %
Peak to peak active power ripples during grid voltage sag	0.8 kW	0.8 kW	0.6 kW	0.015 kW
Percentage ripple in active power during grid voltage sag (%)	21 %	21 %	15.8 %	0.39 %
Frequency tracking time during grid frequency deviation	120 ms	120 ms	-	60 ms

3.5 Conclusion

This chapter presents an integrated control strategy for a grid-tied photovoltaic system, which mitigates the grid current harmonics and power oscillations under distorted grid voltage conditions. The proposed control strategy consists of an advanced proportional multi-resonant (APMR) controller with a compensator for grid voltage sags (CGVS). Additionally, an adaptive step size incremental conductance (ASINC) MPPT is implemented to achieve fast-tracking speed and negligible steady-state oscillations under different atmospheric conditions. The APMR controller consists of two parallel resonant compensator blocks of which one block is used to improve the tracking of the fundamental component of grid current and the other block is used to suppresses the selected harmonic components. The CGVS operation along with APMR eliminates the active and reactive power ripples under the unbalanced voltage sags. Moreover, the proposed control strategy improves the frequency adaptability of the grid-tied PV system under grid frequency variations. To verify the effectiveness of the proposed control strategy, a laboratory prototype is designed and tested at 3.8 kW PV power. It is observed from the experimental responses that the harmonic compensation capability with the proposed APMR controller is superior as compared to the conventional PI and conventional PMR controller. Moreover, the proposed control strategy is more effective in reducing the grid current harmonics and eliminating the power ripples under distorted grid voltage conditions as compared to conventional PMR controller. The proposed control strategy also improves the frequency adaptability in case of grid frequency variations.

The proposed PLL-based control strategy is developed for a grid-tied PV system in this chapter. The proposed control strategy achieves superior harmonic reduction and power ripple reduction capability using s a PLL unit for synchronization. In the following chapters, the thesis focuses on the development of the grid-tied PV system using a PLL-less control strategy, considering the benefits of PLL-less approach. In Chapter 4, the reduction of grid current harmonics and elimination of active and reactive power ripples are addressed using a PLL-less control strategy for a grid-tied PV system.